J. Fluid Mech. (1996), *vol.* 317, *pp.* 21–71

Experimental study of the fine-scale structure of conserved scalar mixing in turbulent shear flows. Part 1. $Sc \gg 1$

By KENNETH A. BUCH, JR.† AND WERNER J. A. DAHM
Department of Aerospace Engineering, The University of Michigan, Ann Arbor, MI 48109-2118, USA

(Received 20 January 1995 and in revised form 1 November 1995)

We present results from an experimental investigation into the fine-scale structure associated with the mixing of a dynamically passive conserved scalar quantity on the inner scales of turbulent shear flows. The present study was based on highly resolved two- and three-dimensional spatio-temporal imaging measurements. For the conditions studied, the Schmidt number ($Sc \equiv \nu/D$) was approximately 2000 and the local outer-scale Reynolds number ($Re_\delta \equiv u\delta/\nu$) ranged from 2000 to 10000. The resolution and signal quality allow direct differentiation of the measured scalar field $\zeta(\boldsymbol{x}, t)$ to give the instantaneous scalar energy dissipation rate field $(Re\,Sc)^{-1}\boldsymbol{\nabla}\zeta\cdot\boldsymbol{\nabla}\zeta(\boldsymbol{x}, t)$. The results show that the fine-scale structure of the scalar dissipation field, when viewed on the inner-flow scales for $Sc \gg 1$, consists entirely of thin strained laminar sheet-like diffusion layers. The internal structure of these scalar dissipation sheets agrees with the one-dimensional self-similar solution for the local strain–diffusion competition in the presence of a spatially uniform but time-varying strain rate field. This similarity solution also shows that line-like structures in the scalar dissipation field decay exponentially in time, while in the vorticity field both line-like and sheet-like structures can be sustained. This sheet-like structure produces a high level of intermittency in the scalar dissipation field – at these conditions approximately 4% of the flow volume accounts for nearly 25% of the total mixing achieved. The scalar gradient vector field $\boldsymbol{\nabla}\zeta(\boldsymbol{x}, t)$ for large Sc is found to be nearly isotropic, with a weak tendency for the dissipation sheets to align with the principal axes of the mean flow strain rate tensor. Joint probability densities of the conserved scalar and scalar dissipation rate have a shape consistent with this canonical layer-like fine-scale structure. Statistics of the conserved scalar and scalar dissipation rate fields are found to demonstrate similarity on inner-scale variables even at the relatively low Reynolds numbers investigated.

1. Introduction

The mixing of two or more fluid components at the molecular level in turbulent shear flows plays a dominant role in a wide range of practical problems, especially when chemical reactions occur between the constituents. Such problems can often be formulated in terms of an appropriately defined dynamically passive conserved scalar field quantity $\zeta(\boldsymbol{x}, t)$. This refers to any identifiable scalar variable that is solely advected by the fluid and diffuses relative to the fluid, but which is neither created nor

† Present address: Sandia National Laboratories, Diagnostic and Reacting Flow Department, PO Box 969, MS 9051, Livermore, CA 94551-0969, USA.

destroyed within the flow and which does not directly affect the flow field. Examples include inert tracers such as dyes or molecular species being mixed in liquid or gaseous flows, the mixing of two or more inert fluid streams, or even, of particular interest for combustion problems, the evolution of elemental mixture fraction variables in chemically reacting flows. Often in engineering problems, the particular objective involves obtaining comparatively rapid rates of mixing, and for this reason practical problems generally focus on scalar mixing in turbulent flows. In many of these, and especially when a chemical reaction is involved, it is processes occurring at the molecular diffusion scales in the conserved scalar field that are crucial in determining the outcome of the mixing process.

The investigation reported here is aimed at identifying the physical characteristics of the fine-scale structure associated with the molecular mixing of conserved scalars in turbulent flows. In particular, the results presented address the scalar mixing process in uniform-density turbulent flows and, consistent with this restriction, are confined only to the mixing of scalar quantities for which the diffusivity is constant. We are, furthermore, concerned solely with the mixing of dynamically passive scalar quantities, so that the evolution of the underlying velocity field is completely uncoupled from the progress of mixing in the scalar field. Finally, the work addresses only the molecular mixing due to gradients in the conserved scalar field, and does not deal with diffusion due to temperature gradients or pressure gradients, which can be important in certain specialized problems.

The results presented are from highly resolved two- and three-dimensional spatio-temporal imaging measurements of the fine structure of large Schmidt number conserved scalar mixing in the fully developed self-similar far field of a turbulent shear flow. The spatial and temporal resolution of these measurements reach beyond the local strain-limited molecular diffusion scale of the flow, allowing spatial derivatives involved in determining the local instantaneous scalar gradient field $\nabla\zeta(\boldsymbol{x}, t)$ to be accurately determined. The resulting two-dimensional scalar dissipation rate fields $\nabla\zeta\cdot\nabla\zeta(\boldsymbol{x}, t)$ are then examined to discern the underlying fine-scale structural features of the molecular mixing process in turbulent shear flows.

The scope of this investigation is aimed principally at addressing four specific questions. First, is there any coherent fine structure associated with the molecular mixing of dynamically passive conserved scalar fields in turbulent flows? Secondly, what are the detailed features of any such characteristic underlying fine structure, and to what extent is this structure describable by simple canonical models? Thirdly, what is the effect of the Schmidt number of any underlying fine-scale structure in the scalar dissipation rate field in turbulent flows? In particular, is there any similarity in the fine structure for $Sc \gg 1$ and $Sc \approx 1$, and equally importantly, what differences are there in these two limits? This issue will be addressed by comparing the results obtained here for $Sc \gg 1$ with those obtained in a companion paper (Buch & Dahm 1996, hereafter referred to as Part 2) presenting analogous experimental results obtained at $Sc \approx 1$. Fourthly, what are the implications of this fine-scale structure of scalar mixing for the equilibrium structure of chemically reacting turbulent flows?

The presentation is organized as follows. Section 2 of this paper summarizes a number of basic concepts essential to the present formulation of the molecular mixing process in turbulent flows. Section 3 briefly describes the experimental facility. Following this, §4 describes the measurement technique used, the spatial and temporal resolution achieved as well as the signal quality attained, and summarizes certain details of the data reduction procedures used. In §5 we then present results from these imaging measurements documenting the fine-scale structure for $Sc \gg 1$, including

representative maps of the instantaneous conserved scalar and scalar dissipation fields, and identify the underlying canonical structural elements of the molecular mixing process. Certain statistics associated with the scalar mixing process are presented in §6, and in §7 we examine the internal structure of the canonical diffusion layers noted in §5. Finally, in §8 we discuss these results and summarize the major conclusions drawn from them. Additionally, two appendices provide certain peripheral analyses essential to the results presented here.

2. Basic concepts

Our treatment of mixing is in terms of a generic conserved scalar quantity ζ, the precise physical meaning of which depends on the particular problem at hand. In this section, we summarize concepts associated with the dynamics of scalar fields that are essential to the formation adopted here, as well as in Part 2, and review several hypotheses concerning the fine structure of vorticity and scalar fields in turbulent flows.

2.1. *Dynamics of the scalar mixing process*

In any conserved scalar field $\zeta(\boldsymbol{x}, t)$ satisfying the requirements specified above, the local scalar value can change only through advection of the scalar by the fluid and molecular diffusion of the scalar relative to the fluid. Assuming a constant scalar diffusivity, the scalar field then satisfies the conservative advection-diffusion equation

$$\left[\frac{\partial}{\partial t}+\boldsymbol{u}\cdot\boldsymbol{\nabla}-\frac{1}{Re\,Sc}\nabla^2\right]\zeta(\boldsymbol{x}, t)=0. \tag{2.1}$$

Here, all variables are dimensionless through normalization by reference length and velocity scales, l^* and u^*, and reference scalar value ζ^*. In (2.1), the only parameter appearing explicitly is the dimensionless scalar diffusivity $(Re\,Sc)^{-1}$, where $Re\,Sc$ is the product of the Reynolds number $Re \equiv (u^* l^*/\nu)$ and the Schmidt number $Sc \equiv (\nu/D)$, with ν and D the vorticity and scalar diffusivities, respectively. However, the velocity field $\boldsymbol{u}(\boldsymbol{x}, t)$ in (2.1) is governed by its own transport equation

$$\boldsymbol{\nabla}\cdot\boldsymbol{u}(\boldsymbol{x}, t)=0, \tag{2.2a}$$

$$\boldsymbol{\nabla}\times\boldsymbol{u}(\boldsymbol{x}, t)=\boldsymbol{\omega}(\boldsymbol{x}, t), \tag{2.2b}$$

$$\left[\frac{\partial}{\partial t}+\boldsymbol{u}\cdot\boldsymbol{\nabla}-\frac{1}{Re}\nabla^2\right]\boldsymbol{\omega}(\boldsymbol{x}, t)=\boldsymbol{\omega}\cdot\boldsymbol{\nabla}\boldsymbol{u}, \tag{2.2c}$$

where we have taken the fluid density and viscosity to be constant. Equation (2.2*c*) introduces the Reynolds number separately and, as a consequence, the scalar field in (2.1) depends on both Re and Sc independently.

If the normalization in (2.1) and (2.2) is by the local outer scales $l^* \equiv \delta$ and $u^* \equiv u$ which characterize the local mean shear in the flow, the resulting local outer-scale Reynolds number is $Re_\delta \equiv (u\delta/\nu)$. When viewed on these outer scales, the scalar field structure will be dependent on both Re and Sc. However, if the normalization is by the local inner scales $l^* \equiv \lambda_\nu$ and $u^* \equiv (\nu/\lambda_\nu)$, where $\lambda_\nu \sim \delta Re_\delta^{-3/4}$ is the local strain-limited vorticity diffusion lengthscale (see §7), then the resulting inner-scale Reynolds number is unity. In this case, provided the scale separation between the local inner and outer scales is sufficiently wide (i.e. provided Re_δ is sufficiently large), the velocity field in (2.1) and (2.2) should, when viewed on the inner scales, be independent of the outer-scale Reynolds number. Since the outer variables appear in (2.1) and (2.2) only through the

Reynolds number, $\boldsymbol{u}(\boldsymbol{x}, t)$ and $\zeta(\boldsymbol{x}, t)$ would therefore also be independent of the outer-scale variables and, furthermore, would also be independent of the particular turbulent flow. It is in this sense that the fine-scale structure of the mixing and energy dissipation processes, when viewed on the inner scales of high Reynolds number turbulent flows, are believed to be largely universal, that is independent of the Reynolds number and the particular flow. As a consequence, when viewed on the inner scales, the fine-scale structure of the conserved scalar field would then depend only on the Schmidt number Sc.

Generally speaking, the inner scales of turbulent flows at Reynolds numbers sufficiently high for the scale separation to unequivocally allow this presumed universal structure to establish itself are beyond the reach of current experimental resolution capabilities. Ultimately, the finest experimental resolution attainable places a limit on the highest Reynolds number at which such fine structure measurements can be meaningfully made. In the experimental investigation undertaken here, the objective is to obtain very highly resolved measurements of the fine structure scales of the molecular mixing process in turbulent flows at conditions for which the Reynolds numbers are believed to be high enough that this universality is at least largely established. In this sense, the overall nature of the fine structure seen here, as well as its detailed features documented in these measurements, are believed to be largely generic to high Reynolds number conserved scalar mixing in turbulent flows, and not specific to the particular Reynolds numbers or the particular flows in which the measurements were obtained.

To discern the fine structure of mixing in a conserved scalar field $\zeta(\boldsymbol{x}, t)$, it is useful to define the scalar energy per unit mass $\frac{1}{2}\zeta^2(\boldsymbol{x}, t)$, analogous to the kinetic energy per unit mass $\frac{1}{2}|\boldsymbol{u}|^2(\boldsymbol{x}, t)$. From (2.1) the scalar energy then follows the transport equation

$$\left[\frac{\partial}{\partial t}+\boldsymbol{u}\cdot\boldsymbol{\nabla}-\frac{1}{Re\,Sc}\nabla^2\right]\tfrac{1}{2}\zeta^2(\boldsymbol{x}, t) = -\frac{1}{Re\,Sc}\boldsymbol{\nabla}\zeta\cdot\boldsymbol{\nabla}\zeta(\boldsymbol{x}, t), \tag{2.3}$$

where the same conservative advection-diffusion operator as in (2.1) appears on the left-hand side. The right-hand side is strictly negative, and gives the local instantaneous rate at which molecular diffusion reduces non-uniformities in the scalar energy field. For this reason, $\chi(\boldsymbol{x}, t) \equiv (Re\,Sc)^{-1}\boldsymbol{\nabla}\zeta\cdot\boldsymbol{\nabla}\zeta(\boldsymbol{x}, t)$ is often referred to as the local instantaneous scalar energy dissipation rate per unit mass of fluid, or simply the scalar dissipation.

From (2.1) the exact transport equation for the scalar gradient vector $\boldsymbol{\nabla}\zeta(\boldsymbol{x}, t)$ appearing in the dissipation on the right-hand side of (2.3) is

$$\left[\frac{\partial}{\partial t}+\boldsymbol{u}\cdot\boldsymbol{\nabla}-\frac{1}{Re\,Sc}\nabla^2\right]\boldsymbol{\nabla}\zeta(\boldsymbol{x}, t) = -(\boldsymbol{\nabla}\zeta\cdot\boldsymbol{\epsilon})-(\boldsymbol{\nabla}\zeta\times\tfrac{1}{2}\boldsymbol{\omega}), \tag{2.4}$$

where the same conservative advection-diffusion operator appears on the left. On the right, the first term describes the change in both magnitude and direction of the scalar gradient vector due to the local strain rate tensor $\boldsymbol{\epsilon} \equiv \frac{1}{2}(\boldsymbol{\nabla u}+\boldsymbol{\nabla u}^T)$ associated with the underlying velocity field. The second term gives the pure rotation of the scalar gradient vector with the fluid vorticity in (2.2) but produces no change in the gradient magnitude.

The scalar dissipation in (2.3) is simply the magnitude squared of the scalar gradient vector in (2.4), and therefore follows the transport equation

$$\left[\frac{\partial}{\partial t}+\boldsymbol{u}\cdot\boldsymbol{\nabla}-\frac{1}{Re\,Sc}\nabla^2\right]\tfrac{1}{2}(\boldsymbol{\nabla}\zeta\cdot\boldsymbol{\nabla}\zeta) = -(\boldsymbol{\nabla}\zeta\cdot\boldsymbol{\epsilon}\cdot\boldsymbol{\nabla}\zeta)-\frac{1}{Re\,Sc}\boldsymbol{\nabla}(\boldsymbol{\nabla}\zeta):\boldsymbol{\nabla}(\boldsymbol{\nabla}\zeta). \tag{2.5}$$

In the first term on the right, the symmetric contraction simply selects the normal component of the strain rate tensor along the local scalar gradient vector direction, giving $-\epsilon_{\nabla\zeta\nabla\zeta}(\nabla\zeta\cdot\nabla\zeta)$. The remaining components of the strain rate tensor thus act only to change the gradient vector orientation, but do not affect its magnitude. Therefore, this first term simply accounts for the reduction in scalar gradient magnitude due to extensional straining along the gradient direction or, conversely, the increase in dissipation resulting from compression of the scalar gradient. The second term on the right in (2.5) is strictly negative and gives the reduction in dissipation due to diffusional cancellation of gradients in the scalar field.

The discussion above briefly outlines the dynamics governing the mixing process for an arbitrary conserved scalar quantity. In dealing with specific problems, sometimes the diffusivity D of the scalar quantity being mixed is small in comparison with the vorticity diffusivity ν; in other words, the Schmidt number ($Sc \equiv \nu/D$) is large. Examples include the mixing of fine particles such as soot or oil droplets in the atmosphere, the mixing and reaction of aqueous acid–base solutions, or the mixing of various components in a wide range of liquid-phase chemical, pharmaceutical, and industrial processes. However, in many other problems of practical interest, the vorticity and scalar diffusivities are roughly the same, giving $Sc \approx 1$. Examples of this latter type include the mixing of two different inert gases and the evolution of the elemental mixture fraction in gaseous reaction flows. Here we address the fine-scale structure of the mixing of $Sc \gg 1$ conserved scalars; a companion paper (Part 2) addresses the fine structure of $Sc \approx 1$ conserved scalar fields. The remaining class of problems, namely those for which $Sc \ll 1$, is also of interest in certain specialized problems, including mixing in plasmas, but is not addressed here.

2.2. *Fine-structure hypotheses for the vorticity field in turbulent flows*

The notion of a continuous cascade of kinetic energy in high Reynolds number turbulent flows from low-wavenumber velocity fluctuations toward increasingly isotropic higher wavenumbers, at which the energy is ultimately dissipated into heat, has been the cornerstone of turbulent flow theory since its earliest descriptions by Richardson (1920) and Taylor (1935). Kolmogorov (1941) placed this physical picture on a mathematical foundation by introducing the hypothesis of a universal isotropic homogenous statistical distribution for the small scales of high Reynolds number turbulent flows. While experimental results in a wide range of turbulent flows have corroborated some of the implications of Kolmogorov's formulation, there is ample evidence that the predictions of this theory are incorrect for higher moments of the velocity differences. For example, from Kolmogorov's formulation the normalized structure functions of all orders n and their corresponding spectra, when expressed in dissipation variables, should be universal for separation distances r within the inertial range. Instead, measurements at relatively high Reynolds numbers (e.g. Batchelor & Townsend 1949; Gibson, Stegen & Williams 1970; Van Atta & Chen 1970; Van Atta & Yeh 1975; Anselmet *et al.* 1984) imply a dependence on both n and r, especially for large values of n, suggesting that the vorticity and dissipation are distributed within the flow in a more 'spotty' manner than the space-filling distribution implicit in Kolmogorov's (1941) formulation.

Numerous modifications to Kolmogorov's original hypothesis have been introduced to account for this spatial 'spottiness' of the vorticity and dissipation fields. These can be grouped into two types. The first are essentially probabilistic and centre on various largely *ad hoc* assumptions for the distribution of dissipation rates. These so-called intermittency models include, for example, the 'log-normal model' of Kolmogorov

(1962), Obukhov (1962), Novikov & Stewart (1964), and Gurvich & Yaglom (1967); the 'β-model' of Frisch, Sulem & Nelkin (1978); the 'Γ-model' of Andrews & Shivamoggi (1989); the 'fractal model' of Mandelbrot (1974, 1976); the 'multi-fractal model' of Frisch & Parisi (1985), Prasad & Sreenivasan (1990), Sreenivasan (1991), and Meneveau & Sreenivasan (1991); as well as various other 'breakage models'. Borgas (1992) gives a critical review of the class of intermittency models.

The second group, more directly relevant to the present work, consists of physically rooted models based on specific canonical pictures for vortical structure of the dissipative scales. Fine-structure models of this type can be traced back to Burgers (1948, 1950). He considered simple solutions for the fine structure of the vorticity field as sheets or lines of finite thickness established by a balance between the competing effects of strain and diffusion of vorticity. Townsend (1951) showed that sheet-like and line-like structures can evolve, from arbitrary initial vorticity distributions, as special cases for locally planar and axisymmetric strain rate fields. (The term 'sheet-like' will be used here to describe structural features that have one major dimension much smaller than the other two. By comparison, the term 'line-like' refers to features that have one major dimension much larger than the other two.) In both cases, the equilibrium vorticity thickness λ_ν scales with the diffusivity ν and the local compressive strain rate ϵ as $\lambda_\nu \sim (\nu/\epsilon)^{1/2}$. Townsend hypothesized that the fine-scale vortical structure of turbulent flows can be modelled as such sheets or lines passively superimposed on the mean flow, from which he computed the kinetic energy spectrum that would result from a random distribution of such vortex sheets, as well as the spectrum for a random distribution of vortex lines. A slightly better fit with experimentally measured spectra was obtained for the vortex sheet model, and Townsend argued that the strain rate field is more favourable to the formation of vortex sheets than vortex lines (see also Betchov 1956). Corrsin (1962) proposed a somewhat similar model in which the energy dissipation was localized in such randomly distributed vortex sheets, with thicknesses of the order of the Kolmogorov scale and separations of the order of the integral scale. Tennekes (1968) developed a similar model, but based on a random distribution of vortex lines having diameters of the order of the Kolmogorov scale and separations of the order of the Taylor scale.

Direct experimental measurements of fine structure of the vorticity vector field in turbulent flows are beyond current laboratory diagnostic capabilities. However, Kuo & Corrsin (1972) made an early indirect attempt to experimentally assess these different fine-scale structure models of the dissipative scales in turbulent flows. From two-point measurements of velocity in a turbulent flow, they tried to distinguish among three canonical pictures for the underlying fine-scale vortical structure, namely 'sheets', 'lines', and 'blobs'. Their tentative conclusion was that the fine scales were more likely to be line-like than either sheet-like or blob-like. Betchov (1974), however, concluded from four-point measurements that the intermittency resulted from distorted vortex sheets, rather than vortex lines. More recently, using direct numerical simulations of moderate Reynolds number turbulent flows, many numerical studies have been undertaken to discern the fine structure of such flows. These have generally involved simulations of forced or decaying homogenous isotropic turbulent flow in periodic domains. In one of the earliest numerical studies, Siggia (1981) found numerous examples of vortex lines and sheets, as well as blobs, in the vorticity field. The highest values of vorticity were concentrated in line-like structures, in apparent agreement with Kuo & Corrsin's earlier experimental results. Kerr (1985) also concluded from his simulation that the vorticity is concentrated in lines and not in sheets. Yamamoto & Hosokawa (1988) also found the regions of most concentrated vorticity confined to

line-like structures, with diameters of the order of the Kolmogorov scale and lengths typically of the order of the Taylor scale. This would appear to lend support to Tennekes' model of the dissipative scales, but Yamamoto & Hosokawa caution that only a relatively small fraction of the total dissipation occurs within these line-like structures. She, Jackson & Orszag (1990) and others have also confirmed that the highest values of the vorticity are organized into such line-like structures, while lower values show no apparent structure.

2.3. *Fine-structure hypotheses for the scalar field*

Not long after the introduction of Kolmogorov's universal similarity hypotheses for the fine structure of the vorticity field in turbulent flows, it was recognized that certain aspects of this theory were applicable to the fine structure of scalar fields. Obukhov (1949) and Corrsin (1951) argued from this perspective that molecular diffusion would smooth gradients in the scalar field at scales smaller than the finest vortical scale, thereby setting the finest scalar and vorticity scales, λ_D and λ_ν, equal. Batchelor (1959), however, recognized that when the scalar diffusivity D is significantly smaller than the vorticity diffusivity ν, namely when $Sc \gg 1$, the uniform strain rate ϵ over regions much smaller than λ_ν provides a mechanism for sustaining scalar gradients over lengthscales $\lambda_D \ll \lambda_\nu$. In this case, the limiting scale in the scalar field results from a competition between the compression due to the strain field and the thickening due to the diffusion of the scalar, giving $\lambda_D \sim (D/\epsilon)^{1/2}$ with the consequence that $\lambda_D = \lambda_\nu Sc^{-1/2}$. In contrast to this, when $Sc \ll 1$ Batchelor, Howells & Townsend (1959) suggested that the strain rate is irrelevant in setting the finest lengthscales in the scalar field. Gibson (1968*a*, *b*), on the other hand, argued on largely geometrical grounds that, regardless of the relevant magnitudes of ν and D, the strain–diffusion competition always sets the finest lengthscale, giving $\lambda_D \sim (D/\epsilon)^{1/2}$ for all Sc.

It is noteworthy that this picture of a strain–diffusion balance setting the finest lengthscale in the $Sc \gg 1$ conserved scalar field is precisely the mechanism in Burgers' and Townsend's solutions of vortex sheets and lines as the canonical fine-structure elements for the vorticity field in high Reynolds number turbulent flows. As a consequence, these same canonical pictures of sheets and lines are also candidates for the fine structure of the $Sc \gg 1$ conserved scalar fields. However, the possible relevance of these topologies for characterizing the scalar dissipation field in $Sc \approx 1$ turbulent mixing is much less obvious. In particular, when the Schmidt number is close to unity, the lengthscale λ_ν on which gradients in the vorticity and strain rate fields occur is effectively the same as the lengthscale λ_D that would result from a strain–diffusion balance of the type described above. As a consequence, it might be expected that the assumption of a uniform strain rate field over regions significantly larger than λ_D, which is inherent in the line-like and sheet-like models, would not be valid under these conditions. Moreover, even if such a line-like or sheet-like scalar dissipation structure were to form momentarily, the fact that the vorticity is non-uniform over lengthscales of order the thickness of the structure suggests that it might quickly become distorted. It is thus much more difficult to argue on purely conceptual grounds that there should be any such simple structure in the dissipation field for $Sc \approx 1$ conserved scalars.

As is the case for the vorticity field, there have also been a number of numerical simulations aimed at identifying the fine structure of scalar fields in turbulent flows. Such studies have dealt almost exclusively with $Sc \approx 1$ scalars, since then the resolution demands imposed by the finest gradient lengthscale arising in the scalar field are no more severe than those already imposed by the vorticity field. These simulations have also primarily addressed the mixing in homogenous isotropic turbulent flows in

periodic domains. One of the first such studies, by Kerr (1985), concluded that large values of the scalar gradient occurred in sheets wrapped around the line-like vorticity structures. Kerr also found that the scalar gradient tended to align normal to the vorticity and along the most compressive component of the strain rate. Ashurst *et al.* (1987) used Kerr's simulation as well as computations by Rogers & Moin (1987) in a detailed study of the alignment between the vorticity, the scalar gradient, and the principal strain rate axes. In the vicinity of the line-like vortical structures, they observed that the strain field tended to be nearly two-dimensional, having large extensional and compressional principal components, with a significantly smaller intermediate component, that tended to be extensional. The vorticity showed a tendency to align with this intermediate component, corresponding to the most extensional component of the background strain field, while the scalar gradient strongly aligned with the most compressive component. From a two-dimensional inviscid simulation, Gibson, Ashurst & Kerstein (1988) showed that the scalar gradient tended to be largest in those regions where it most closely aligned with the largest compressive principal strain axis. Eswaran & Pope (1988) studied the decay of the scalar field in homogenous turbulent flow, and Yeung, Girimaji & Pope (1989) examined the statistics of a diffuse layer centred on a material surface advected with the flow. Their results indicate that, at early times, before the layer folds over onto itself and begins to interact with itself, the internal structure takes on a self-similar form.

2.4. *Previous $Sc \gg 1$ conserved scalar measurements*

As was the case for the small scales in the vorticity field, experimental studies of the fine-scale structure of $Sc \gg 1$ conserved scalar fields in turbulent flows have also been limited. This is primarily due to two obstacles. First, determination of the true scalar gradient vector field $\nabla\zeta(\boldsymbol{x}, t)$ and the associated scalar dissipation rate field $\nabla\zeta \cdot \nabla\zeta(\boldsymbol{x}, t)$ requires simultaneous measurement of the conserved scalar field in all three spatial dimensions. Owing to the difficulties in making differentiable scalar field measurements in more than one or two dimensions, the dissipation has instead generally been approximated from measurements of lower-dimensional projections of the true scalar gradient field. Secondly, since the dissipation rate field is obtained from derivatives of the measurement conserved scalar field data, the resolution in both space and time, as well as the signal quality, must be sufficiently high to permit accurate differentiation of the measured data.

An early attempt to simultaneously measure all three gradient vector components was made by Prasad & Sreenivasan (1990). They rapidly swept a laser sheet through a turbulent flow and acquired laser-induced fluorescence images at high speed to obtain a series of planar conserved scalar field measurements, estimating the separation between their resulting scalar field planes to be about four Kolmogorov scales. With $Sc \approx 2000$ in their measurements, this gives the interplane separation as 175 Batchelor scales. Based on their measurements (see their figures 14 and 15), these authors conclude that their scalar dissipation fields consist of local singularities of varying strengths, and thus describe these fields using multifractal analyses (e.g. Meneveau & Sreenivasan 1991). The difficulties in resolving the smallest gradient lengthscales are typical of $Sc \gg 1$ scalar field measurements, and have restricted most investigations of the fine structure of conserved scalar fields in turbulent flows to gaseous mixing, where $Sc \approx 1$ and thus the resolution requirements are not as severe. Accordingly, those investigations will be reviewed in Part 2.

The present results are from very highly resolved measurements of the presumably universal fine structure of $Sc \gg 1$ conserved scalar mixing in turbulent flows. These

experiments are based on two-dimensional laser-induced fluorescence imaging measurements, but the in-plane resolution achieved is significantly finer than the local scalar gradient lengthscale estimate in the flow. This addresses the second of the two obstacles mentioned above; however, the results obtained allow direct access to only two of the three gradient vector components. Nevertheless, in assessing various statistical features of the resulting scalar dissipation fields, this missing gradient component can still be accounted for by a general procedure (Dahm & Buch 1989).

3. Experimental facility

The present measurements of $Sc \gg 1$ conserved scalar mixing were conducted in the self-similar far field of an axisymmetric coflowing turbulent jet at local outer-scale Reynolds numbers Re_δ ranging from 2000 to 10000. In this class of turbulent shear flows, a jet issues with momentum flux J_0 into an unconfined coflowing stream moving at a constant speed U_∞. In these experiments, the local scalar field value $\zeta(\boldsymbol{x}, t)$ was defined as the jet-fluid mixture fraction, and determined from the aqueous concentration of an inert water-soluble laser fluorescent dye (disodium fluorescein) carried by the jet fluid. The Wilke–Chang method gives the diffusivity D for dilute aqueous solutions of this dye at room temperature as 4.82×10^{-6} m^2 s^{-1}, and Ware *et al.* (1983) give a value of 5.2×10^{-6} m^2 s^{-1}, giving respective values for the Schmidt number as 2075 and 1920.

The coflowing turbulent jet was formed by issuing water containing a small amount of dye (typically around 3×10^{-5} M) through a highly contracting contoured nozzle into a coflowing ambient stream. Both the jet and the ambient fluids were fixed to pH $\approx$ 11 by the addition of NaOH. The flows were established in a low-turbulence-level gravity-driven blow-down Bernoulli tunnel with a 30 cm × 30 cm × 120 cm test section. The test section consisted of four 120 cm × 33 cm × 0.75 in. Lucite windows in a stainless steel frame with a 40 cm × 40 cm × 1.25 in. Lucite window on the bottom, allowing optical access on-axis as well as from all four sides. The upper reservoir was a 110 cm × 110 cm × 110 cm tank that emptied into a 240 cm × 120 cm × 90 cm lower reservoir through the test section.

An 8 in. electro-pneumatically positioned butterfly valve controlled the flow through the test section. The valve angle was set by a current signal supplied to the valve controller from a 12-bit D/A board in a laboratory computer. To determine the time-varying valve angle necessary to maintain a constant velocity in the test section, the unsteady Bernoulli equation was solved using a calibration for the pressure drop across the valve as a function of the valve angle and flow rate, and the initial water levels in each reservoir. The resulting valve angle versus time was read from a file during each run to maintain a constant coflow velocity. LDV measurements showed that with this procedure the resulting test section velocity drifted no more than 5% from the desired value over the entire run time. Test section velocities as low as a few millimetres per second and as high as 75 cm s^{-1} could be established in this facility. The flow entered the test section through a rapid 11:1 area ratio contraction that effectively reduced the boundary layers at the test section entrance to negligible thickness. LDV measurements also determined the test section flow velocity fluctuations as a function of settling time in the upper reservoir. With increasing settling time, the turbulence intensity decreased below the 0.2% noise limit of the LDV. Longer settling times led to higher intensities, apparently due to thermal stratification in the upper reservoir.

The jet plenum was a 4 in. ID × 41 in. Lucite cylinder with an end-plate containing a fitting for the pneumatic drive. The Lucite nozzle had a 5.5 in. overall length and a

5 mm interior exit diameter. The exterior of the nozzle was tapered to give a thin lip at the exit. The very large area ratio contraction (400:1) yielded a uniform exit velocity profile that allowed calculation of the jet exit momentum flux J_0 directly from the measured mass flow rate in the plenum. A pneumatic drive system was used to issue the dye-containing plenum fluid through the nozzle. This consisted of a micrometer-controlled variable-throat metering valve held at sonic conditions with a constant upstream pressure that produced a constant and carefully controlled mass flow rate of air into the jet plenum. A solenoid valve was used to initiate the air flow into the plenum. A ballast tank, positioned upstream of the metering valve, maintained the upstream pressure during the starting transient.

4. Diagnostic technique and experimental conditions

4.1. *The LIF measurement technique*

The jet-fluid mixture fraction was determined by measuring the intensity of laser-induced fluorescence from dye-containing fluid in a small region of the flow though which a collimated laser beam was rapidly swept. A 100 mm Vivitar macro lens collected the fluorescence emitted by the dye at image ratios as low as 1:1. The fluorescence intensity was measured with a 256×256 high-speed planar photodiode array (EG&G Reticon MC9256/MB9000) having a centre-to-centre pixel spacing of 40 μm. Figure 1 is a schematic representation of the data acquisition system used to collect and store the serial fluorescence output signal from the imaging array. The array was driven by an externally generated TTL clocking signal at pixel rates up to 11 MHz, corresponding to acquisition of up to 142 data planes per second. The serial analog output signal from the array formatter consisted of a sampled-and-held voltage proportional to the integrated fluorescence intensity incident on each pixel between successive samplings of the pixel. This signal then passed to a high-speed data acquisition system (RCI Trapix 55/256) via a programmable digital port interface. An 8-bit A/D converter, using externally programmed gain and offset values, digitized the signal and ported it into 16 MB of high-speed dual-ported memory from which it was subsequently written to a disk.

For the range of dye concentrations used in these experiments, the response of the dye is nearly linear, providing a direct relationship between the measured fluorescence signal and the dye concentration for a given local laser beam power. The spectrum of fluorescence emission was sufficiently separated from the laser excitation lines to allow Mie scattering from particles in the flow to be removed by an optical filtre [HOYA O(G)]. The multi-line emission (principally 488.0 nm and 514.5 nm) from a 5 W Ar^{++} laser excited the dye fluorescence in the flow. The decay time of the resulting laser-induced fluorescence is of the order of nanoseconds, and thus much faster than any relevant fluid dynamic timescales associated with the turbulent flow or the scalar mixing process. The laser beam was focused to a waist at the centreline of the jet, and imaging measurements of the beam showed that the 1/e beam thickness typically ranged from 115 to 130 μm over the entire extent of the measurement plane.

Since each photodiode in the array integrated the dye fluorescence over the entire time between successive samplings of that pixel, the effective temporal resolution was greatly increased by sweeping the collimated laser beam through the flow rather than imaging from a fixed laser sheet. This reduced the effective integration time for each pixel to the time the beam spent in the pixel's field of view – a reduction of more than

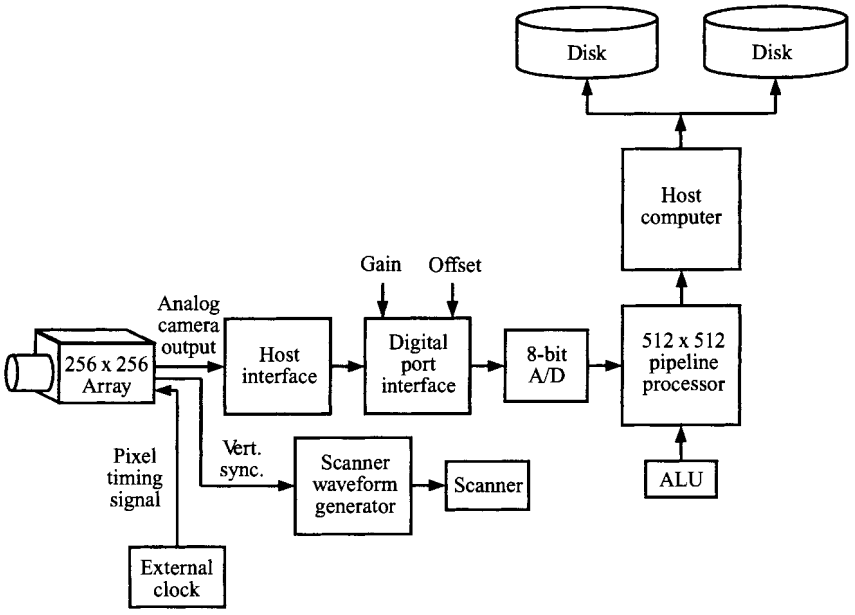

FIGURE 1. Schematic of the data acquisition system showing the photodiode array, timing signal path and image data path through the user-interface to the data storage system.

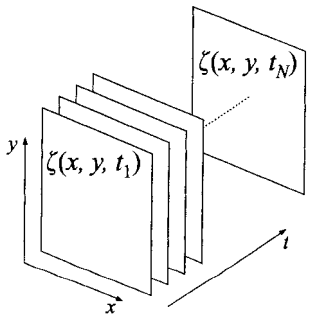

FIGURE 2. Structure of the three-dimensional, 256^3, spatio-temporal data volumes for the $Sc \gg 1$ measurements. Each volume is composed of up to 256 individual two-dimensional spatial data planes, each containing 256×256 highly resolved point measurements of the local conserved scalar value ζ.

two orders of magnitude. A very low-inertia mirror mounted on a fast galvanometric scanner (General Scanning GA120DT) controlled the beam sweep through the measurement area. To avoid resonant oscillations of the mirrors, the scanner was driven by a frequency-limited ramp waveform from a programmable function generator, which in turn was slaved back to the master clock driving the photodiode array.

The laser beam was attenuated along its propagation path through the scalar field as dye molecules in the flow absorbed energy from the beam and emitted a fraction of this as fluorescence. Since the fluorescence intensity is, in part, proportional to the local power of the laser beam, the local fluorescence intensity from any point in the scalar field depends not only on the local dye concentration but also on the integrated

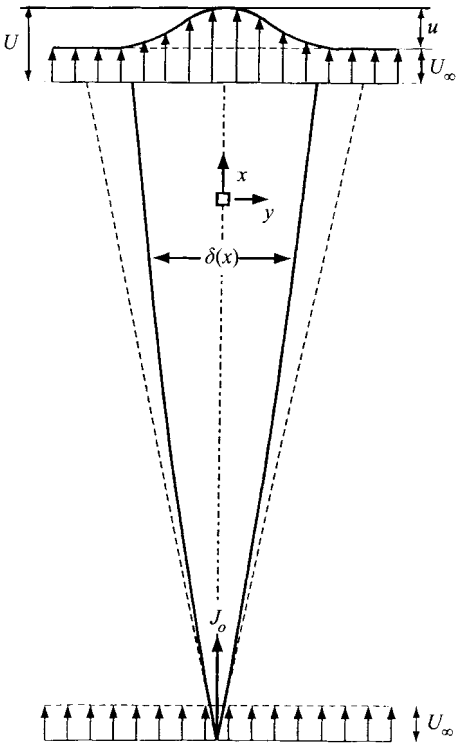

FIGURE 3. Schematic showing the typical size and location of the measurement area for the $Sc \gg 1$ experiments. Note that the measured region is significantly smaller than the local jet width $\delta(x)$ and is typically of the order the local inner scale $\lambda_\nu(x)$.

Run designation	Sc	$Re_\delta \equiv u\delta/\nu$	J_o (N)	U_∞ (m s^{-1})	x (m)	(x/ϑ)
A10279	2075	3500	0.006	0.025	1.0	18
A09130	2075	2500	0.003	0.018	1.0	18
A10070	2075	2100	0.009	0.18	1.0	106
A10080	2075	2900	0.022	0.38	1.0	144
A10110	2075	9600	0.048	0.078	1.0	20

TABLE 1. Experimental conditions for the $Sc \gg 1$ experiments

attenuation of the laser beam up to that point. This attenuation can be precisely accounted for if the true dye concentration is known at one point along each beam path, but no such dye reference location is available in these measurements. However, determination of the scalar gradient field involves only differences in the measured fluorescence intensity between adjacent pixels. Since the typical change in laser beam power due to attenuation from one pixel to the next is very small in comparison with the typical change in scalar value between pixels, the scalar gradient field $\nabla\zeta(\boldsymbol{x}, t)$ could be accurately obtained even though the attenuation effects were ignored. As indicated in figure 2, each of these measurements produced a data volume composed of up to 256 successive highly resolved two-dimensional spatial data planes arranged sequentially in time. Each data plane is, in turn, composed of an array of 256×256 individual point measurements of the local conserved scalar field value $\zeta(\boldsymbol{x}, t)$.

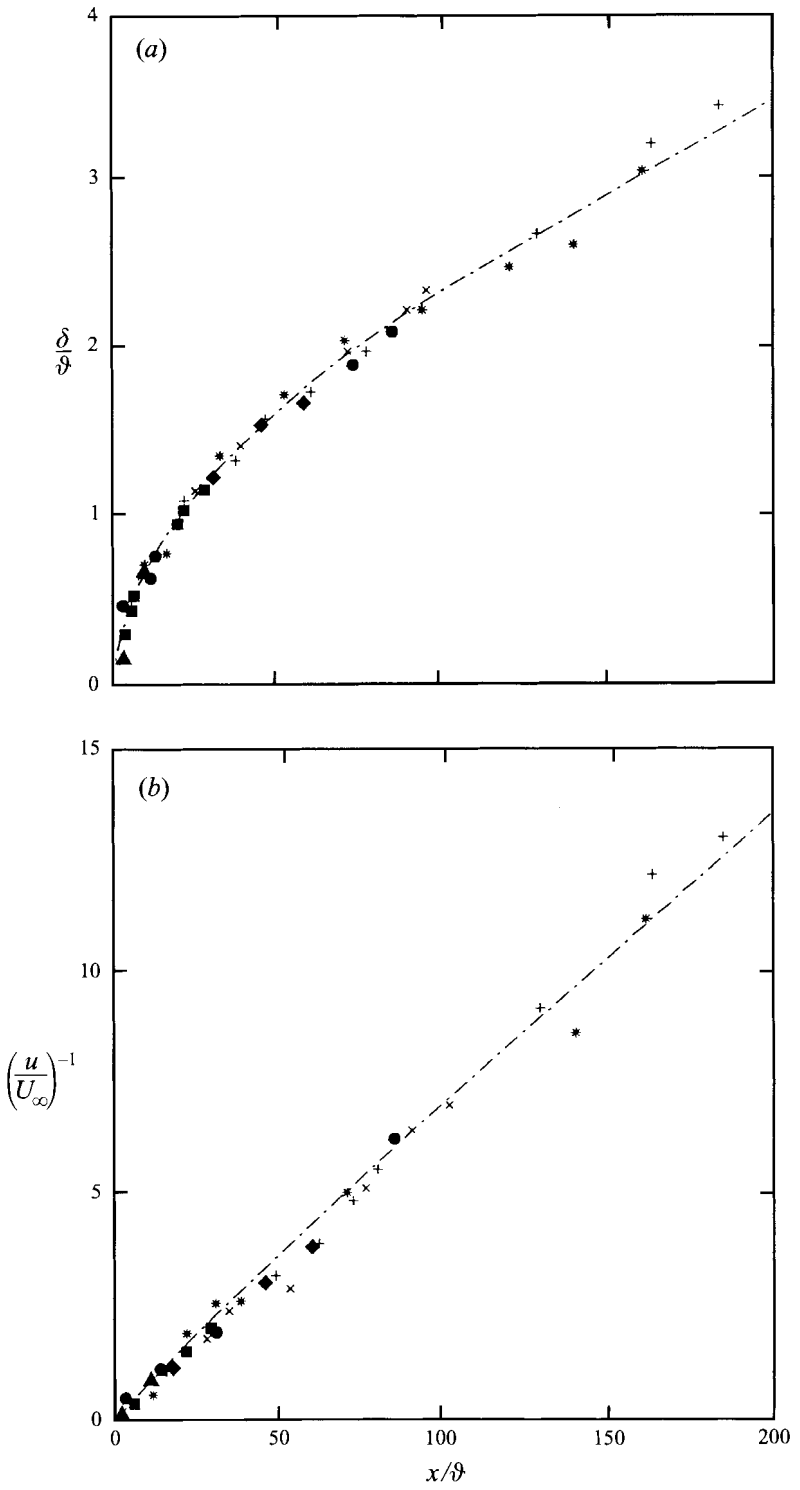

FIGURE 4. Similarity scaling functions for the local jet width (δ/ϑ) and the local centreline excess velocity (u/U_∞) as functions of the proper dimensionless downstream coordinate (x/ϑ). Data of Biringen (1975). (*a*) Local outer scale width $\delta(x)$, (*b*) local centreline excess velocity $u(x)$.

4.2. *Flow conditions*

Table 1 summarizes the flow conditions for which results are presented. All the data were collected at an axial distance of $x = 1.0$ m, corresponding to 200 jet nozzle exit diameters downstream of the source. In the proper dimensionless downstream similarity variable (x/ϑ) for axisymmetric coflowing jets (see §4.3), this fixed axial distance corresponds to $18 \leqslant (x/\vartheta) \leqslant 144$, depending on the particular flow conditions. As a result, all of these measurement locations lie well within the fully developed self-similar far field of the flow and in between the jet-like and wake-like algebraic similarity limits (see §4.3).

Figure 3 shows the approximate region in the flow covered by each data plane. Each plane was centred on the jet axis, with one spatial dimension corresponding to the axial flow direction and the other to the radial direction. It is essential to note that the region in the flow covered by each data plane is considerably smaller, in both directions, than the local jet width δ, and is typically of the order of the local strain-limited vorticity diffusion scale λ_ν. For the results presented, the spatial extent of the data planes is as small as $\frac{1}{18}\delta$ in both directions, and in no case are they larger than $\frac{1}{7}\delta$. With the local Reynolds number ranging from 2100 to 9600, the size of the data planes relative to the local inner scale ranges from $0.8\,\lambda_\nu$ to $2.5\,\lambda_\nu$. As a result, provided these Reynolds numbers are high enough for a sufficient separation of scales to exist between the local outer and inner scales, δ and λ_ν respectively, the results obtained for the scalar dissipation rate field should be representative of the generic fine structure of large Schmidt number mixing in turbulent shear flows.

4.3. *Spatial and temporal resolution*

The result of any point measurement of the local conserved scalar field value is a spatio-temporal average representing the integral of the true scalar field values over the pixel volume $\Delta x \times \Delta y \times \Delta z$ and the time Δt during which the pixel collects the fluorescence from this volume. However, if the scalar field varies no more than linearly in space within this pixel volume, then from the mean value theorem, the measured average obtained will be equal to the true scalar field value at the centre of the measurement volume. If, furthermore, the scalar field also varies only linearly in time over the pixel integration period, then the resulting time average will be the true scalar field value at the centre of the integration period. Accurate point measurements of the scalar field thus require the spatial and temporal resolution corresponding to each pixel to be at least comparable to the smallest local length- and timescales on which gradients appear in the local conserved scalar field.

The finest gradient lengthscale sustainable in the vorticity field results from a competition between the thinning effect of the local strain rate ϵ and the thickening effect of molecular diffusion. Dimensional reasoning requires the local equilibrium lengthscale in the vorticity field established by this strain–diffusion balance to scale as $\lambda_\nu \sim (\nu/\epsilon)^{1/2}$. A similar strain–diffusion balance sets the finest lengthscale on which scalar gradients can be sustained by the flow, though in this case molecular diffusion occurs at the scalar diffusivity D, giving the strain-limited equilibrium lengthscale in the scalar field as $\lambda_D \sim (D/\epsilon)^{1/2}$. Exact self-similar solutions of the Navier–Stokes and conserved scalar transport equations, giving detailed descriptions of the strain–diffusion equilibrium processes in the vorticity and conserved scalar field, are presented in §7. Here we note only that, in response to a change in the local strain rate ϵ, over a timescale of the order of the inverse strain rate the lengthscales λ_ν and λ_D approach their new strain-limited values either exponentially in time from above or as

square root in time from below, thereby continuously tending to remain in equilibrium with the strain rate.

In turbulent flows, the local strain rate ϵ will vary in both space and time, and classical inertial-range scalings indicate that the highest local strain rates should scale as $\epsilon \sim (u/\delta)\, Re_\delta^{1/2}$. Here, u and δ are the local outer velocity and length scales that characterize the local shear in the flow. In the coflowing jet, these scales are the local flow width $\delta(x)$ (defined here as the full width between the points where the mean scalar profile reaches 5% of the centreline value) and the centreline excess velocity $u \equiv (U - U_\infty)$, respectively, as indicated in figure 3. This gives the smallest local lengthscales on which gradients can be sustained in the vorticity and scalar fields as

$$\lambda_\nu/\delta \sim Re_\delta^{-3/4}, \quad \lambda_D/\delta \sim Sc^{-1/2}\, Re_\delta^{-3/4}. \tag{4.1a, b}$$

Measurements by Dowling & Dimotakis (1991), as well as earlier estimates by Hill (1978, 1980), suggest that the proportionality constant is roughly 25. Note that with $Sc \approx 2000$ the finest gradient lengthscale that must be resolved in the conserved scalar field is approximately 45 times smaller than that in the vorticity field.

Estimates for the spatial and temporal resolution requirements λ_D and λ_D/U, respectively, involve the outer-scale variables u and δ. In axisymmetric coflowing turbulent jets these variables follow non-algebraic far-field similarity scalings first noted by Maczynski (1962). These scalings can be easily understood by recognizing that as $(u/U_\infty) \to \infty$, the effect of the coflow should become locally negligible and the flow should approach the scaling for an axisymmetric turbulent jet issuing into a quiescent medium. For this flow, the local jet width and centreline velocity are

$$\delta \sim x, \quad u \sim (J_o/\rho_\infty)^{1/2}\, x^{-1}, \tag{4.2a, b}$$

where J_o is the jet source momentum flux and ρ_∞ is the ambient fluid density. In the opposite limit, as $(u/U_\infty) \to 0$, the momentum flux integral in terms of the excess velocity $u \equiv (U - U_\infty)$ becomes identical to that obtained for wake in terms of the deficit velocity. In this case, self-similarity requires the simple algebraic scalings

$$\delta/\vartheta \sim (x/\vartheta)^{1/3}, \quad u/U_\infty \sim (x/\vartheta)^{-2/3}, \tag{4.3a, b}$$

where ϑ denotes the invariant momentum radius of the flow given by

$$\int_0^\infty \frac{u(r)}{U_\infty}\left[1 + \frac{u(r)}{U_\infty}\right] 2r\, \mathrm{d}r = \frac{J_o}{\pi \rho_\infty U_\infty^2}. \tag{4.4}$$

In terms of x/ϑ, the wake-like limit in (4.3*a*, *b*) corresponds to $x/\vartheta \to \infty$. At the other extreme, the jet-like limit in (4.2*a*, *b*) corresponds to $x/\vartheta \to 0$, and can be written in terms of ϑ as

$$\delta/\vartheta \sim x/\vartheta, \quad u/U_\infty \sim (x/\vartheta)^{-1}. \tag{4.5a, b}$$

Equations (4.3) and (4.5) suggest that over the entire range $0 < x/\vartheta < \infty$, the axisymmetric coflowing turbulent jet will follow a non-algebraic similarity scaling of the form

$$\delta/\vartheta \sim f_1(x/\vartheta), \quad (u/U_\infty)^{-1} \sim f_2(x/\vartheta), \tag{4.6a, b}$$

with f_1 and f_2 satisfying these asymptotic limits. Measurements by Reichardt (1964) and Biringen (1975) have confirmed these scalings and give the functions f_1 and f_2 as shown in figure 4.

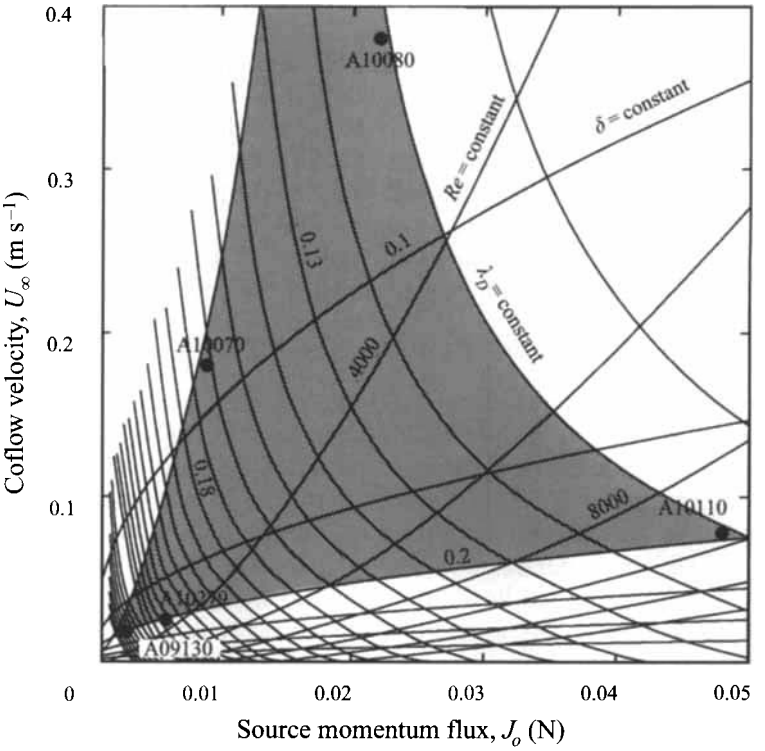

FIGURE 5. Spatial resolution map for the $Sc \gg 1$ measurements. Shown are contours of constant local molecular diffusion scale λ_D, jet width δ, and local Reynolds number Re_δ. The shaded region denotes the conditions for which the molecular diffusion scale is smaller than the maximum dimension of each projected pixel volume in the flow. The limit on the jet width is to ensure that the unconfined scalings in §4.3 apply to the flow.

Run designation	λ_D (μm)	$\Delta x, \Delta y$ (μm)	Δz (μm)	λ_D/U (ms)	Δt (ms)	ΔT (ms)
A10279	246	80	250	5.8	0.14	8.5
A09130	316	43	190	10.5	0.12	380
A10070	162	48	130	0.8	0.042	190
A10080	111	48	130	0.27	0.042	190
A10110	111	50	130	0.87	0.17	760

TABLE 2. Resolution estimates for the $Sc \gg 1$ experiments

The scaling laws in (4.1) and (4.6) together with the scaling functions f_1 and f_2 allow estimates to be obtained for the finest spatial and temporal scales, λ_D and λ_D/U respectively, arising in the scalar field $\zeta(\boldsymbol{x}, t)$ in terms of J_o, U_∞, and x. Figure 5 shows the resulting spatial resolution constraints that these measurements must meet. Shown are contours of constant local outer-scale Reynolds number $u\delta/\nu$, local flow width δ, and local strain-limited molecular diffusion scale λ_D at the measurement location $x = 1.0$ m. The shaded area indicates the domain (J_o, U_∞) in which spatially resolved measurements can be obtained, constrained by the following criteria. The lower limit on Re is specified as 2000 and the upper limit on the jet width δ is 20 cm to prevent interference from the test section walls. The minimum allowable λ_D is set by the laser

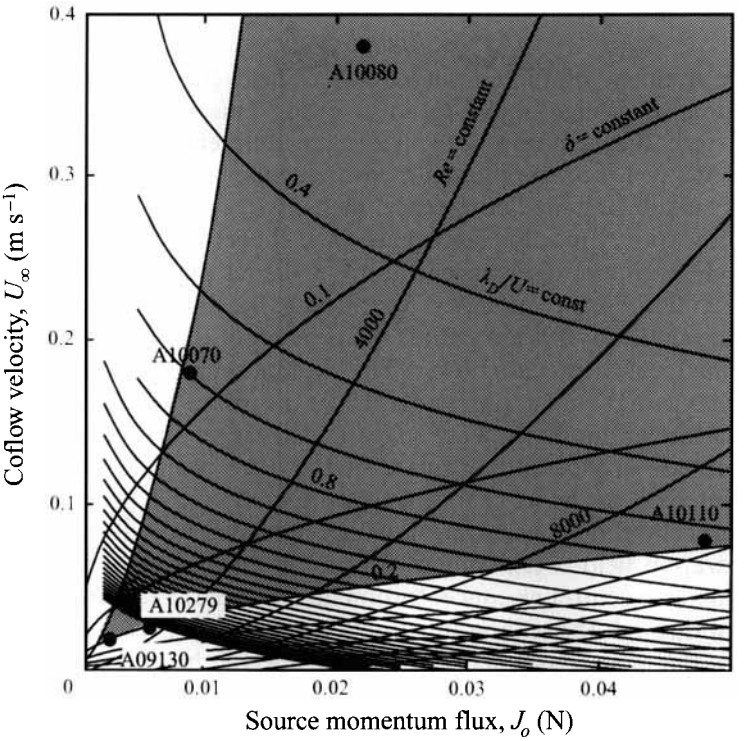

FIGURE 6. Temporal resolution map for the $Sc \gg 1$ measurements. Shown are contours of constant local molecular diffusion scale advection time (λ_D/U), jet width δ, and local Reynolds number Re_δ. The shaded region denotes the conditions for which the molecular diffusion scale is temporally resolved by each pixel measurement.

sheet thickness Δz, since this is the largest dimension of the measurement volume (see §4.1). For each of the experimental conditions listed in table 1, the resulting spatial resolution estimates are listed in table 2. Note that the data are essentially spatially resolved ($\Delta x, \Delta y \ll \lambda_D; \Delta z \approx \lambda_D$) in all the cases presented.

Similarly, figure 6 gives the temporal resolution constraints on these measurements. Shown in this case are contours of the local molecular-diffusion-scale advection time λ_D/U, namely the characteristic time required for the flow to move one strain-limited scalar gradient lengthscale at the mean centreline velocity. Also shown are contours indicating the same constraints on the local Reynolds number and the local flow width as in figure 5. The (J_o, U_∞) range over which temporally resolved measurements can be obtained is shown by the shaded area. For the experimental conditions listed in table 1, the resulting temporal resolution estimates are also listed in table 2. Note that in each case the laser beam diameter, the sweep rate, the pixel size and image ratio set the effective time Δt over which each pixel is illuminated. Temporal resolution constraints require that $\Delta t \ll \lambda_D/U$, as is the case in all of these data. Note that the time ΔT between acquisition of successive data planes is also listed for comparison with the timescale λ_D/U. For all cases except that designated as A10279, the data between successively acquired planes were temporally uncorrelated ($\Delta T \gg \lambda_D/U$) to permit statistical convergence of various quantitative measures of the mixing process. For the case denoted A10279, the inter-plane time is $\Delta T \approx \lambda_D/U$ to allow the temporal evolution of the mixing process to be examined.

4.4. *Signal quality*

Accurate measurement of the conserved scalar field $\zeta(\boldsymbol{x}, t)$ requires not only high resolution but also a high signal-to-noise ratio. This is especially true for these experiments since the resulting data are to be differentiated to obtain the scalar gradient field $\boldsymbol{\nabla}\zeta(\boldsymbol{x}, t)$. For the present measurements, maximizing the signal-to-noise ratio requires maximizing the fluorescence intensity from the jet centreline at the given measurement location. Since the laser power and the jet width are fixed for each case, there is a single optimum dye concentration in the jet plenum that will produce the maximum mean fluorescence intensity. Specifically, the fluorescence intensity obtained at any point along the laser beam path is the product of the local dye concentration in the flow and the local laser beam power. The latter is coupled to the dye concentration through an exponential attenuation integral over the instantaneous concentration field. The integral nature of this dependence suggests that the mean concentration field could be used to provide an accurate estimate of the laser beam attenuation. The mean fluorescence intensity at the jet centreline is computed by this procedure to determine the local mean centreline concentration which maximizes the fluorescence. Since the mean concentration field is self-similar, for any given parameter values the resulting optimum local mean centreline concentration determines the required concentration in the jet plenum through the scaling functions $f_1(x/\vartheta)$ and $f_2(x/\vartheta)$. Following Dahm & Dibble (1988), the mean centreline scalar value is given by

$$\overline{\zeta_m}(x) = \frac{\dot{m}_o}{\rho_\infty U_\infty \vartheta^2}\left\{\frac{f_1^2(x/\vartheta)}{f_2(x/\vartheta)}[I_1 + I_2 f_2(x/\vartheta)]\right\}^{-1}, \tag{4.7}$$

where the integrals I_1 and I_2 are given by

$$I_1 \equiv \int_0^\infty \frac{\bar{\zeta}(\eta)\,\bar{u}(\eta)}{\bar{\zeta}(0)\,\bar{u}(0)} 2\pi\eta\,\mathrm{d}\eta, \quad I_2 \equiv \int_0^\infty \frac{\bar{\zeta}(\eta)}{\bar{\zeta}(0)} 2\pi\eta\,\mathrm{d}\eta, \tag{4.8a, b}$$

with measurements yielding $I_1 \approx 0.103$ and $I_2 \approx 0.254$. This procedure gives the plenum dye concentration required to maximize the signal quality for any given flow conditions.

Once this optimal dye concentration has been found, the signal-to-noise is then fixed by various noise sources inherent in the measurements and data acquisition system. In the present experiments, the limiting noise factor was the switching noise, or *ktc* offset noise, which is proportional to the square root of temperature times the square root of capacitance in the array. This noise was typically about 3000 electrons, or 1 digital signal level. The dark noise, as measured for the array used, was less than 1 digital level. Other noise factors, including thermal noise, are all typically less than the switching noise. By comparison, for the dye concentration obtained by the procedure described above, the fluorescence signal values typically spanned the full 256 digital levels.

4.5. *Data reduction*

The raw fluorescence data resulting from data acquisition were first divided by a measured transfer function which collectively accounts for various non-idealities in the imaging system. For each case in table 1, this transfer function was determined from the average fluorescence intensity measured with a uniform weak dye concentration in the test section. The fixed array noise and any background signal were then subtracted from each of the corrected data planes. The background signal resulted from stray

fluorescence collected by the array while the beam was outside the measurement area, and was approximated from measurements with a uniform weak dye concentration in the test section.

From the resulting scalar field data, the in-plane components of the scalar gradient vector field $\nabla\zeta(\boldsymbol{x}, t)$ were computed using linear central differences on a 3×3 template. For two-dimensional spatial data such as these, this can be done in two coordinate frames: one being the natural frame coincident with the pixel rows and columns, and the second being a rotation of the first through $\frac{1}{4}\pi$. This allows two separate approximations for the gradient vector components, each of which makes use of the measured scalar field values at only four of the eight neighbouring points. Averaging the two approximations for each of the components then makes unbiased use of the scalar field values at all eight points. The resulting expression for the two-dimensional scalar dissipation at point (i,j) is

$$(\nabla\zeta\cdot\nabla\zeta)_{i,j} = \left[\frac{1}{4\Delta}(\zeta_{i+1,j}-\zeta_{i-1,j})+\frac{1}{8\Delta}(\zeta_{i+1,j+1}+\zeta_{i+1,j-1}-\zeta_{i-1,j-1}-\zeta_{i-1,j+1})\right]^2$$
$$+\left[\frac{1}{4\Delta}(\zeta_{i,j+1}-\zeta_{i,j-1})+\frac{1}{8\Delta}(\zeta_{i+1,j+1}+\zeta_{i-1,j+1}-\zeta_{i-1,j-1}-\zeta_{i+1,j-1})\right]^2, \quad (4.9)$$

where Δ is the centre-to-centre pixel spacing in the flow. Similarly, the in-plane scalar gradient vector orientation angle ϑ is given by

$$\tan\vartheta_{i,j} = \frac{[(\zeta_{i,j+1}-\zeta_{i,j-1})+\frac{1}{2}(\zeta_{i+1,j+1}+\zeta_{i-1,j+1}-\zeta_{i-1,j-1}-\zeta_{i+1,j-1})]^2}{[(\zeta_{i+1,j}-\zeta_{i-1,j})+\frac{1}{2}(\zeta_{i+1,j+1}+\zeta_{i+1,j-1}-\zeta_{i-1,j-1}-\zeta_{i-1,j+1})]^2}. \quad (4.10)$$

As is the case for any discrete derivative operator, this eight-point derivative template is equivalent to an implicit filter that offers the additional advantage of somewhat reducing the effects of noise on the gradient vector computations. However, aside from the implicit noise reduction inherent in this derivative, no explicit smoothing or filtering was applied to the resulting gradient vector fields. The results were then normalized by the local inner scales of the flow field, namely $l^* = \lambda_v$ and $u^* = (\nu/\lambda_v)$ and the mean scalar value obtained by averaging over the entire data volume, namely $\zeta^* = \zeta_m$.

5. Structure of the scalar and dissipation rate fields

In this section, we present typical results for the conserved scalar fields $\zeta(\boldsymbol{x}, t)$ and the associated scalar dissipation rate fields $\chi(\boldsymbol{x}, t) \equiv (Re\,Sc)^{-1}\nabla\zeta\cdot\nabla\zeta(\boldsymbol{x}, t)$ obtained from these measurements. The discussion is aimed at identifying the underlying structural features characteristic of the scalar mixing process at the molecular diffusion level. In some instances, several examples are presented from a single experiment to give a clearer indication of the typical range of topological features seen in the dissipation rate fields. Quantitative analyses of these fields are given in subsequent sections.

5.1. *Sample fields*

Figures 7–13 show typical data planes obtained for each of the measurement conditions listed in tables 1 and 2. In each figure, part (*a*) shows an example of an instantaneous conserved scalar field $\zeta(\boldsymbol{x}, t)$, part (*b*) shows the corresponding map of the scalar energy dissipation rate field $\chi(\boldsymbol{x}, t)$ obtained from the in-plane projection of

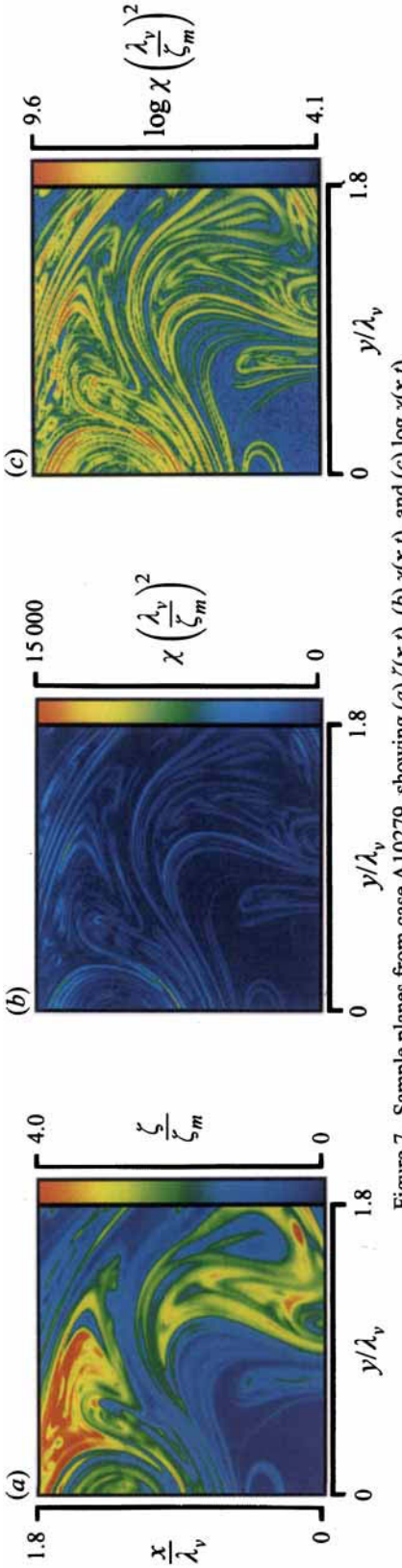

Figure 7. Sample planes from case A10279, showing (*a*) $\zeta(\boldsymbol{x},t)$, (*b*) $\chi(\boldsymbol{x},t)$, and (*c*) $\log\chi(\boldsymbol{x},t)$.

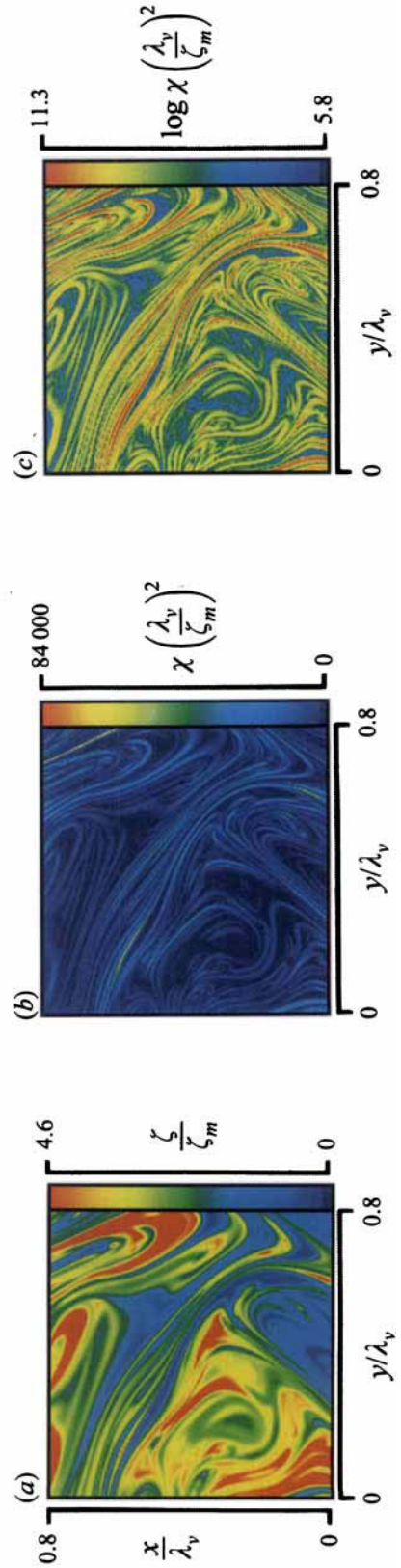

Figure 8. Sample planes from case A09130, showing (*a*) $\zeta(\boldsymbol{x},t)$, (*b*) $\chi(\boldsymbol{x},t)$, and (*c*) $\log\chi(\boldsymbol{x},t)$.

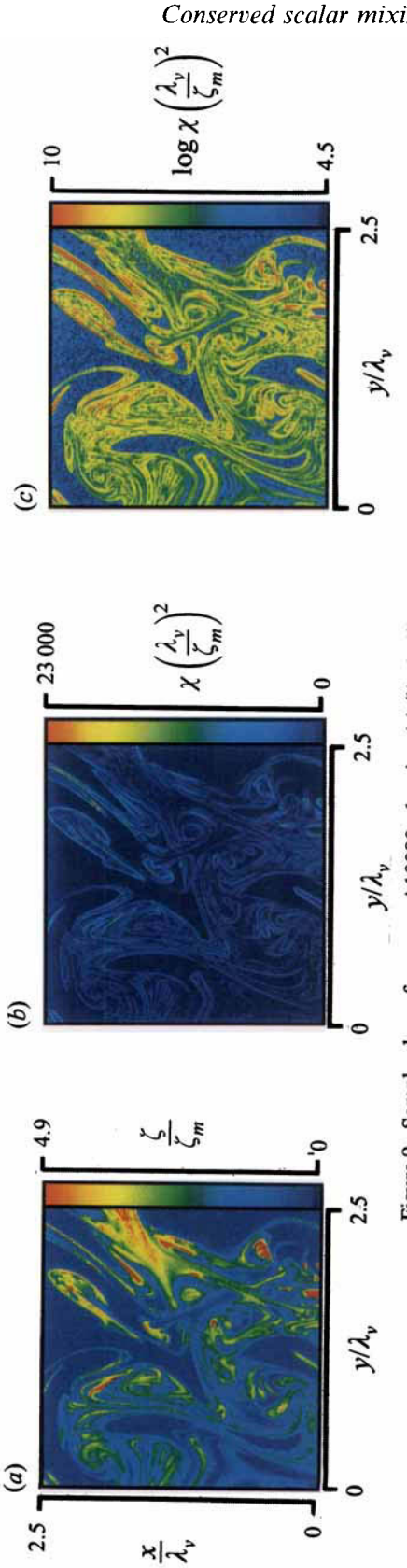

Figure 9. Sample planes from case A10080, showing (*a*) $\zeta(\boldsymbol{x},t)$, (*b*) $\chi(\boldsymbol{x},t)$, and (*c*) $\log\chi(\boldsymbol{x},t)$.

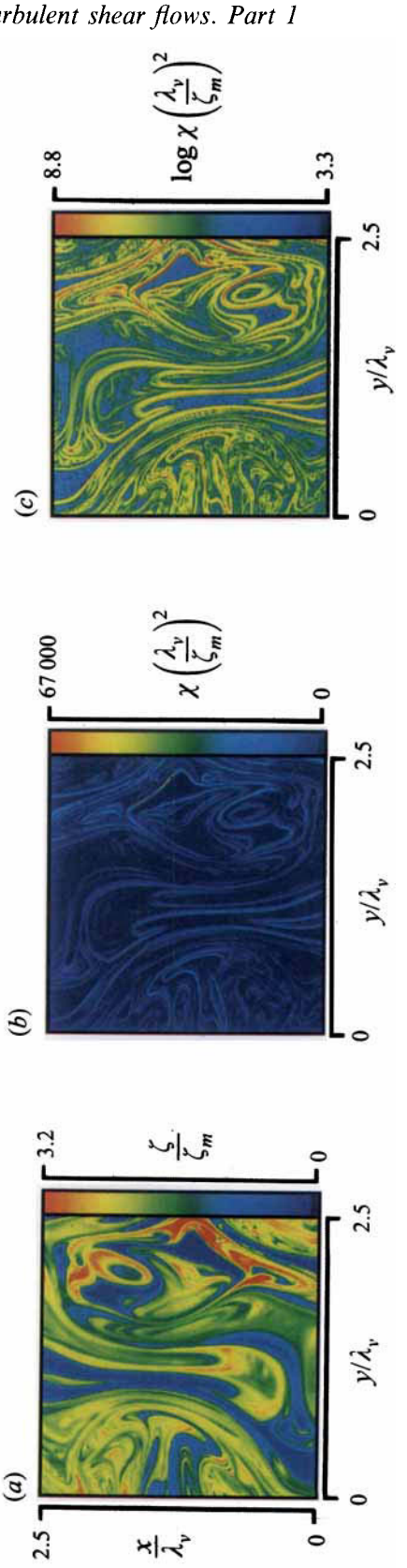

Figure 10. Sample planes from case A10110, showing (*a*) $\zeta(\boldsymbol{x},t)$, (*b*) $\chi(\boldsymbol{x},t)$, and (*c*) $\log\chi(\boldsymbol{x},t)$.

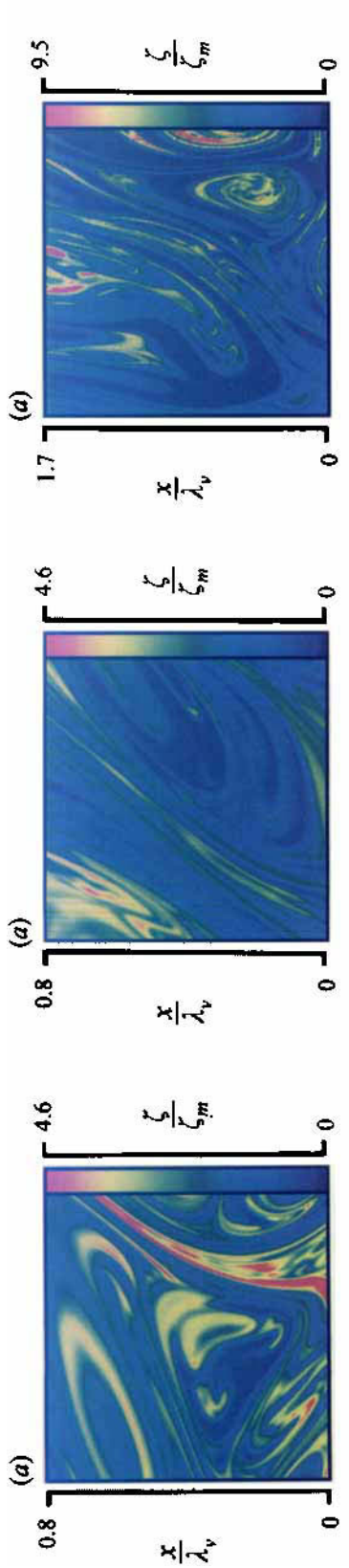

Figure 11. Samples from case A09130, showing (*a*) $\zeta(x,t)$, (*b*) $\log \chi(x,t)$.

Figure 12. Samples from case A09130, showing (*a*) $\zeta(x,t)$, (*b*) $\log \chi(x,t)$.

Figure 13. Samples from case A10070, showing (*a*) $\zeta(x,t)$, (*b*) $\log \chi(x,t)$.

the true scalar gradient vector field, and part (*c*) shows the scaled logarithm of the scalar energy dissipation rate field $\log_e \chi(x, t)$. The logarithmic maps provide more contrast at the low dissipation rates, allowing the structure to be more readily seen, while the linear maps provide a better view of the 'spottiness' of the dissipation rate fields.

In all these figures, the jet centreline runs vertically down the centre of each data plane, though the fact that no consistent directional preferences are apparent in these fields suggests that they are at least approximately isotropic. (This issue is addressed quantitatively in §6). The axes indicate the spatial extent of each data plane in terms of the local strain-limited vorticity diffusion lengthscale λ_ν, obtained as described in §4.3. Note that the relative size of these maps in terms of the local inner variables (x/λ_ν) and (y/λ_ν) is different for each case. A comparison of the relative sizes of the inner lengthscale estimates λ_ν show reasonable agreement with 'eddy-like' structures in the scalar and dissipation fields. Note that the vorticity field structure can of course at best be only qualitatively approximated from the scalar and dissipation field structures seen in these figures; however, the time development afforded by $\Delta T \approx (\lambda_D/u)$ in case A10279 allows some insight into the local dynamics of the flow, and verifies that such intuitive vortical lengthscale estimates inferred from the dissipation field structure in these figures are at least roughly correct. Related to this, it should be noted that estimates of the relative local outer-flow scale δ among all these cases were also in good agreement with the values predicted by the scaling laws in §4.3, suggesting that the flow followed the far-field similarity scalings for axisymmetric turbulent coflowing jets, and therefore also the resulting Reynolds number scalings.

In each part of figures 7–13, the colour bar identifies quantitative values for the variable shown. For the conserved scalar fields $\zeta(x, t)$, each of the 256 different colour levels denotes a narrow range of the local instantaneous conserved scalar value in the flow. In each case, pure blue denotes the lowest range of scalar values, beginning at $\zeta = 0$ and corresponding to pure ambient fluid. The colours ranging from blue to red denote uniformly increasing conserved scalar values, with pure red denoting the highest 0.1% of scalar values seen in that particular data volume. Similarly, for the scalar dissipation rate fields $\chi(x, t)$, pure blue denotes the lowest range of dissipation values, beginning at $\chi = 0$, with the remaining 255 colours ranging from pure blue to pure red denoting linearly increasing dissipation rates. The highest 0.1% of the dissipation rates in the data volume are all mapped to pure red. For the logarithm of the dissipation rate field, $\log_e \chi$, the lowest level (pure blue) denotes zero and very low dissipation rates, and the remaining colours correspond to logarithmically increasing dissipation rates, with pure red denoting the highest 0.1% of the dissipation rate values.

The derivatives computed within each spatial data plane give the projection of the true three-dimensional scalar gradient vector $\nabla\zeta(x, t)$ into the data plane. As a consequence, the instantaneous local dissipation rate values obtained inherently underestimate the magnitude of the true dissipation rate when the scalar gradient vector has a significant out-of-plane component. However, the values obtained nevertheless provide an accurate picture of the structure of the true dissipation field. This will be the case except at relatively rare points where the gradient vector points almost precisely perpendicular to the imaging plane. In this sense, measurements such as these, involving only two space dimensions, are entirely adequate for a study of the structure of conserved scalar mixing in turbulent flows. Moreover, for a known distribution of scalar gradient vector orientations (e.g. under the assumption of isotropy), even statistical measures associated with the magnitude of the true

dissipation rate field can be correctly deduced from the present two-dimensional approximations (as described in §6.4).

5.2. *Structure*

The data in figures 7–13 allow the underlying structural features associated with the fine scales of the molecular mixing of $Sc \gg 1$ conserved scalar fields in turbulent flows to be directly identified. As can be seen in the dissipation rate fields in part (*b*) of each figure, and even more clearly in the logarithmic forms in part (*c*), the scalar dissipation rate field is organized into thin highly intertwined sheet-like strained laminar diffusion layers on which virtually all the dissipation is concentrated. The characterization of the fine-scale structure of the scalar dissipation rate fields as sheet-like (or 'layer-like') stems from the fact that the basic structural features on which nearly all of the dissipation is concentrated typically maintain a planar topology for many local layer thicknesses. In other words, the local radius of curvature of these features is typically much larger than their local thickness.

The fundamentally layer-like canonical fine-scale structure of the $Sc \gg 1$ scalar dissipation field seen in figures 7–13 contrasts sharply with the much wider range of fine-structure topologies seen in the vorticity field from DNS studies. In particular, as noted in §2, the vorticity magnitude field ($\boldsymbol{\omega}\cdot\boldsymbol{\omega}$) is composed of a complex ensemble of line-like and sheet-like structures, as well as a much wider range of more complex topologies that cannot be readily classified into either of these two limiting structures, producing the notorious complexity of vorticity fields in turbulent flows. The fine structure of the scalar dissipation field ($\nabla\zeta\cdot\nabla\zeta$), on the other hand, can be seen from these results to be composed solely of a locally sheet-like topology. In this sense, the fine structure of the scalar gradient field in turbulent flows is considerably simpler than that of the underlying vorticity field, consisting of just a single well-defined canonical structural element. The reasons for this fundamental and far-reaching difference between the fine-structure topologies present in the vorticity and scalar gradient fields are examined in detail in §7. As a result of this difference, while models of the fine structure in the vorticity field are necessarily more complex, the fine structure of the scalar gradient field can apparently be modelled entirely on the basis of this comparatively simple locally sheet-like topology. These scalar dissipation sheets are of course stretched and folded by the underlying vorticity field into the highly intertwined patterns seen in figures 7–13, but apparently maintain their manifestly sheet-like structure.

5.3. *Magnitudes*

Notice also from the linear colour assignments for the scalar dissipation values in p. (*b*) of these figures that high dissipation values occur only rarely and are clearly confined to easily identifiable sheet-like structures. Low dissipation values, corresponding to blue colourings in these same figure panels, cover a much larger volume fraction of the flow but do not allow as clear an identification of their underlying topology. However, the logarithmic colour assignments used in part (*c*) of these figures clearly confirm that even these low dissipation rates are organized into sheet-like molecular diffusion layers. A quantitative assessment of the distribution of dissipation rates, including a correction that accounts for the missing gradient vector component, is given in §6.

5.4. *Similarity*

A feature of this sheet-like fine structure that can be seen, even if only qualitatively for the moment, from the logarithmic forms of the dissipation rate fields is that the internal profile of the scalar dissipation rates within each of these layers appears to be at least

roughly self-similar. Note that the magnitude of the scalar dissipation clearly varies along the length of any given layer (though apparently only rather slowly), and certainly varies between neighbouring layers in the same data plane and among layers in different data planes. However, the dissipation profiles across all of these layers nevertheless appear to have a similar internal shape. A quantitative assessment of the internal structure of these layers is presented in §7, as well as a comparison with the self-similar canonical solutions referred to in §2.

5.5. *Thicknesses*

It is also noteworthy that the thicknesses of the layer-like structures seen in these figures do not appear to vary over a very wide range. Some caution must be exercised in this observation, however, since the dissipation fields shown are obtained from the two-dimensional projection of the true gradient vector into the measurement plane. As a consequence, the out-of-plane component of the gradient vector is not accounted for in these data. The effect of this is that, if a thicker sheet-like structure were oriented largely tangent to the measurement plane, the two-dimensional dissipation obtained would appear to be very low, corresponding to blue values in the colouring scheme used. Since the lower dissipation rates corresponding to the tails of the normal profile across the sheet would then also be coloured blue, the apparent thickness of the layer might be very similar to that of a sheet oriented largely perpendicular to the measurement plane. A quantitative analysis of the distribution of the diffusion layer thicknesses, including a correction based on isotropy that accounts for these orientation anomalies, is given in Part 2, where the larger gradient lengthscale λ_D afforted by $Sc \approx 1$ allows for a more accurate determination.

6. Statistics of the scalar and dissipation rate fields

The conserved scalar measurements and the resulting scalar dissipation rate fields presented in §5 permit detailed analyses of various statistical measures of the molecular mixing process in turbulent flows. This section deals primarily with various probability distributions describing the scalar dissipation field. Many of these distributions serve to quantify various aspects of the fundamentally sheet-like structure of the dissipation field noted in the previous section.

6.1. *Cumulative distributions*

As was noted in figures 7–13, high dissipation rates occupy only a relatively small fraction of each measured data plane. To quantify this 'spottiness' of the dissipation field, figure 14(*a*) shows the fraction of the total data volume in which the local scalar dissipation rate is greater than some threshold value χ, namely

$$A_0(\chi) \equiv \int \mathrm{d}A_{\chi' > \chi} \Big/ \int \mathrm{d}A. \tag{6.1}$$

The is simply the cumulative distribution function for the scalar dissipation rate, c.d.f.(χ). The rapid drop in the c.d.f.(χ) at very low values of χ reflects the fact that the scalar dissipation field is composed primarily of very low values, with high values occurring infrequently. The similarity of the results in figure 14(*a*) is assessed in figure 14(*b*), where each curve is normalized with the corresponding measured median dissipation value $\chi_{50\%}$. It can be seen that the different curves collapse reasonably well to a single and, presumably, quasi-universal curve. Moreover, as can be seen in table

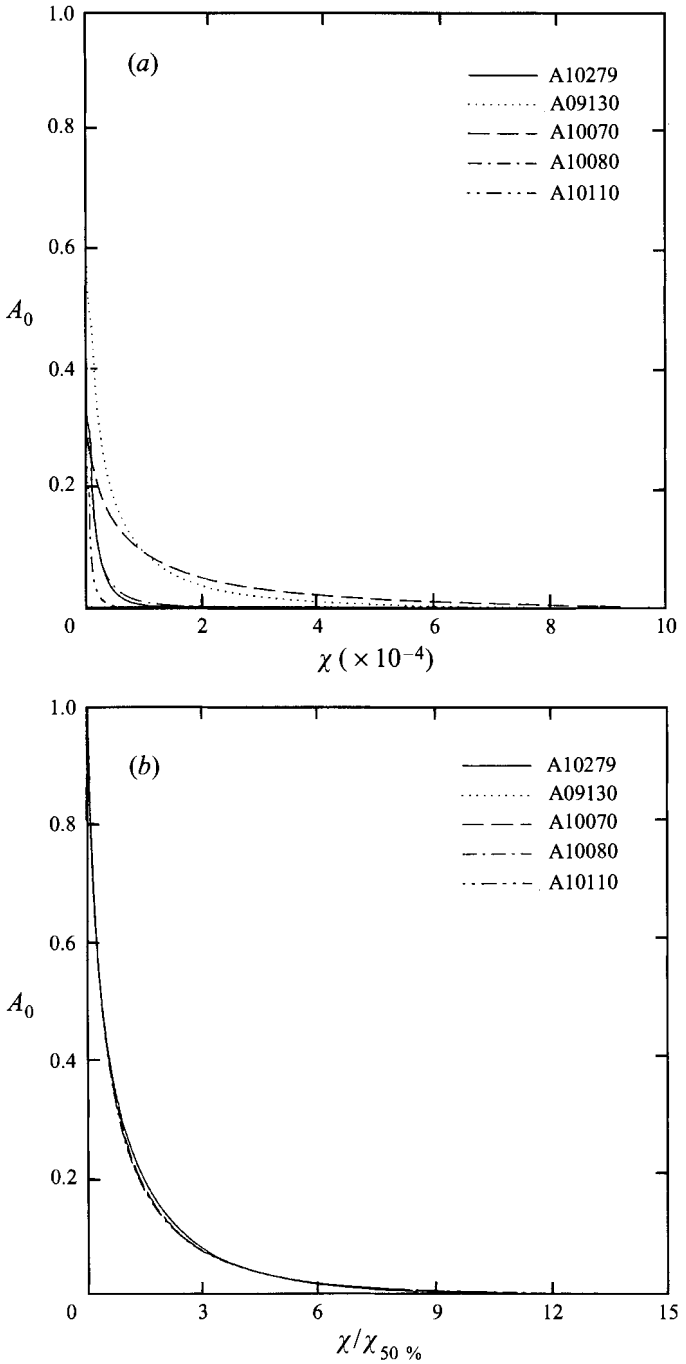

FIGURE 14. (*a*) The cumulative distribution function c.d.f.(χ) of scalar dissipation rates. (*b*) The cumulative distribution function of scalar dissipation rates after normalizing with the corresponding measured mean dissipation value $\chi_{50\,\%}$. Note the collapse onto a single curve which suggests that the distribution of scalar dissipation rates is similar for all the data volumes.

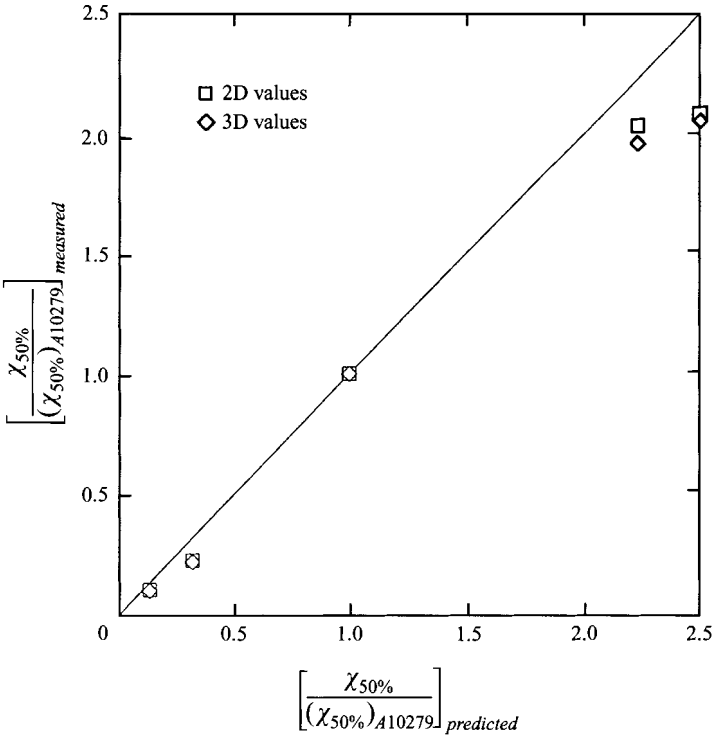

FIGURE 15. Comparison of measured mean χ-values used in the normalizations with the predicted mean dissipation scalings from the outer-flow similarity laws for axisymmetric coflowing turbulent jets.

Run designation	$\left[\frac{\chi_{50\%}}{(\chi_{50\%})_{A10279}}\right]_{predicted}$	$\left[\frac{\chi_{50\%}}{(\chi_{50\%})_{A10279}}\right]_{measured,\,2D}$	$\left[\frac{\chi_{50\%}}{(\chi_{50\%})_{A10279}}\right]_{measured,\,3D}$
A10279	0.134	0.104	0.100
A09130	0.319	0.225	0.219
A10070	1.00	1.00	1.00
A10080	2.23	2.03	1.96
A10110	2.50	2.08	2.05

TABLE 3. Comparison of the measured and predicted mean dissipation rates

3 and in figure 15, although the measured $\chi_{50\%}$ values used in the normalizations in figure 14(*b*) vary over more than a factor of 20, they can be seen to agree quite well with the predicted mean dissipation scalings obtained from the outer-flow similarity laws in (4.6*a*, *b*) and (4.7). Figure 14(*b*) gives a quantitative indication of the spotty nature of the large Schmidt number scalar dissipation fields in turbulent flows.

The integral in (6.1) quantifies how much of the measurement area is associated with a given rate of molecular mixing, but not how much of the mixing is occurring at a given rate. By comparison, the integral

$$A_1(\chi) \equiv \int \chi' \, \mathrm{d}A_{\chi' > \chi} \Big/ \int \chi' \, \mathrm{d}A \tag{6.2}$$

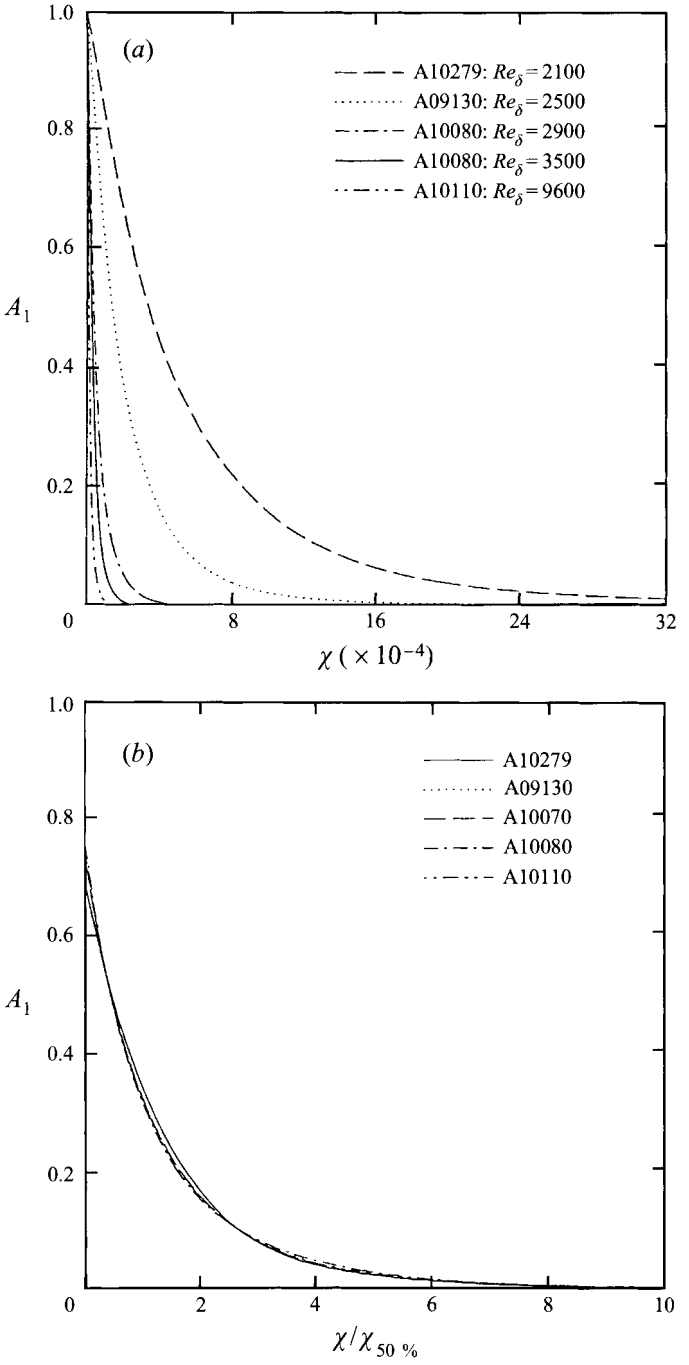

FIGURE 16. (*a*) The cumulative distribution quantifying the fraction of the mixing occurring at a rate greater than some threshold value χ. (*b*) The cumulative distribution shown in (*a*) after normalization with the corresponding mean χ-values. The distributions of mixing rates for all the measurements are similar.

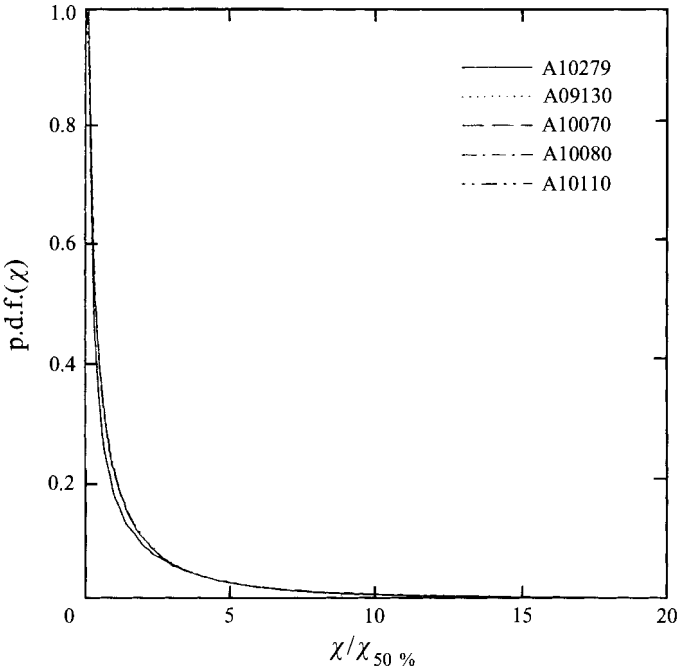

FIGURE 17. The normalized distribution of the two-dimensional scalar dissipation rates p.d.f.(χ) obtained by differentiating the corresponding cumulative distribution functions.

gives the fraction of the mixing occurring at a rate greater than some threshold χ. Figure 16 shows the results obtained for each case and verifies that the increasing mixing rates account for a sharply decreasing fraction of the total mixing. Moreover, note that this measure of the degree of internal intermittency becomes increasingly more compact with increasing outer-scale Reynolds number. These same curves, normalized by the mean χ value, are shown in figure 16(*b*) where it can be seen that the total mixing in all cases consists of a very nearly self-similar distribution of mixing rates. The results in figures 14(*b*) and 16(*b*) allow determination of the fraction of the flow volume that accounts for any given fraction of the total mixing. Note, however, that these distributions still reflect the bias toward low dissipation values resulting from the gradient vector orientation relative to the two-dimensional measurement plane, as discussed in §5. These effects will be accounted for in following sections, and in §6.6 the resulting spatial density of the true three-dimensional scalar dissipation rate fields is quantified.

6.2. *Probability densities*

The fact that the normalized cumulative distributions of the measured dissipation rates collapse to a single curve indicates that the associated probability density functions (p.d.f.s) will also be universal when normalized. The scalar dissipation rate p.d.f.s are obtained here by differentiating the corresponding cumulative distribution functions. Figure 17 shows the results obtained for p.d.f.(χ) from each of the measurements in table 1, where the dissipation values for each case have been scaled by the median value. Note that, with the possible exception of one case, the results obtained all collapse to a single curve. Here the relative infrequency of high dissipation rates noted above manifests itself as a roughly log-normal density function. To assess the deviations from log-normality, figure 18 shows p.d.f.($\log\chi$). The dotted portion of the curve is an extrapolation of the range of dissipation rates accessible by these

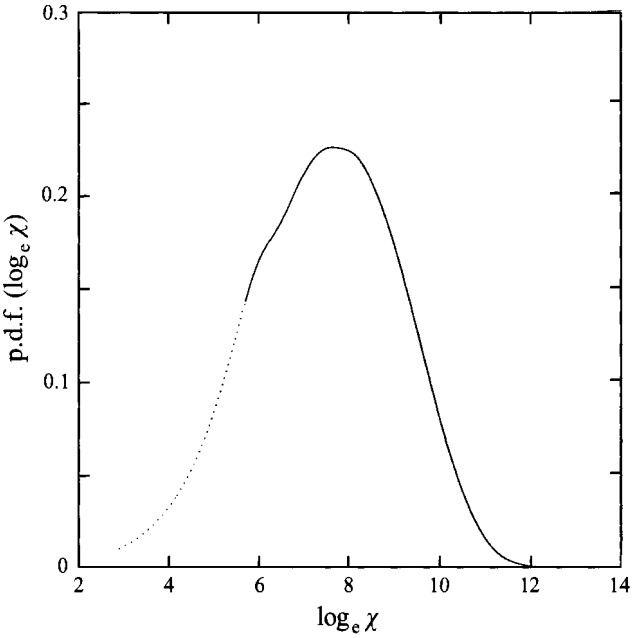

FIGURE 18. The distribution of the logarithm of the two-dimensional scalar dissipation values p.d.f. ($\log_e \chi$) for one of the measurements. The two-dimensional scalar dissipation underestimates the true three-dimensional scalar dissipation, thus overpopulating the low end of the distribution. The dotted line is extrapolated as described in §6.2.

measurements, obtained by a straight line connecting the last non-zero χ value in the linear distribution (figure 17) to zero.

In examining the result in figure 18, it must be kept in mind that the dissipation values shown are from two-component measurements of the true scalar gradient vector, and thus inherently underestimate the true dissipation rates. At least some of the sight asymmetry evident in figure 18 can be expected to be an artifact of this effect. In §6.4, this two-dimensional dissipation distribution will be corrected for the varying scalar gradient vector orientations and the corresponding true three-dimensional scalar dissipation probability density will be presented.

6.3. *Small-scale anisotropy*

Small-scale isotropy is assessed here by testing if the measured scalar gradient vector field $\nabla\zeta(x,t)$ shows any preferred orientation in its distribution $\beta(\vartheta,\varphi)$ of the two spherical orientation angles. Here, ϑ is the azimuth angle in the (x,y)-plane measured from the x-axis, and φ is related to the elevation angle ε from the (x,y)-plane as $\varphi = \frac{1}{2}\pi - \varepsilon$. If the gradient vector is assumed to point with equal probability in all directions (i.e. the scalar gradient vector field is isotropic), then the joint p.d.f. of ϑ and φ is given by

$$\beta(\vartheta,\varphi) = \frac{1}{4\pi}\sin\varphi. \tag{6.3}$$

The projection of the gradient vector into any measurement plane will produce a uniform distribution of the azimuth angle ϑ within that plane. The measured distribution of in-plane gradient vector orientation angles ϑ for two typical data volumes are shown in figure 19. Notice that the spikes in these distributions occur at precisely regular intervals and with an extremely high degree of symmetry in their

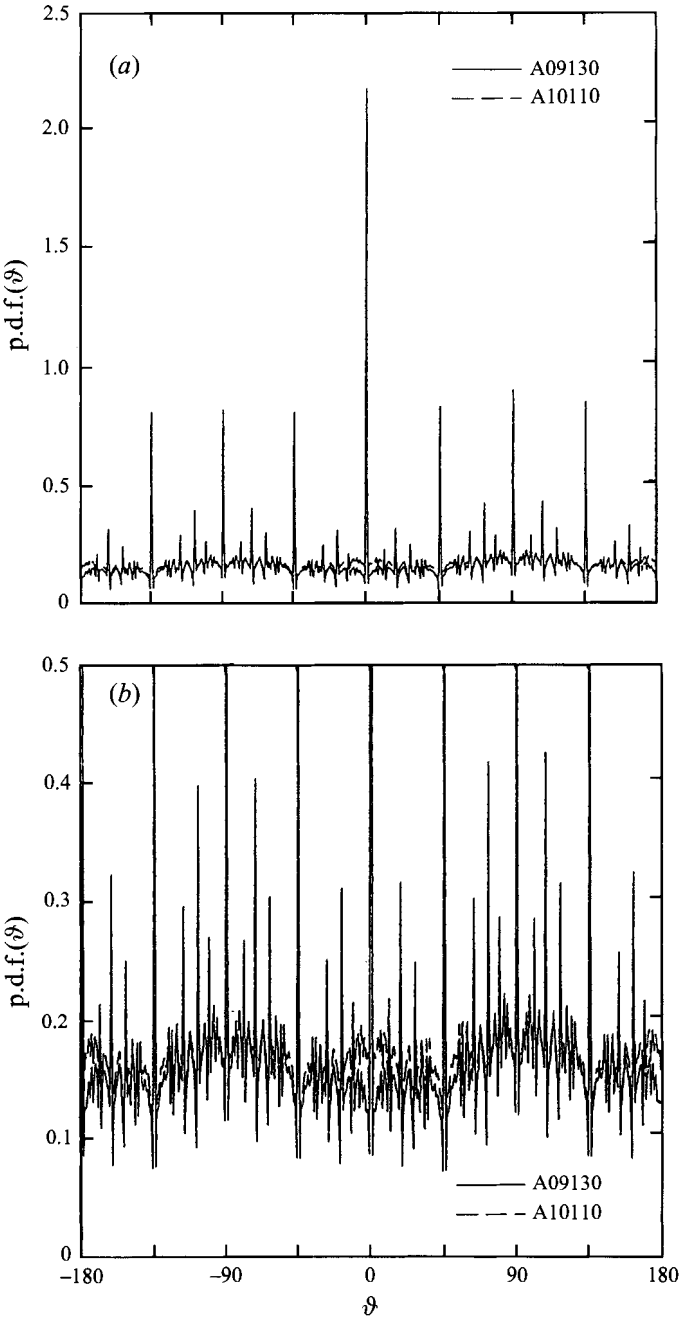

FIGURE 19. (*a*) The distribution of scalar gradient orientation angles p.d.f.(ϑ) for two measurement volumes. The curves are coincident, demonstrating that the peaks are an artifact of the discrete nature of the data and are therefore repeatable. (*b*) The distribution of scalar gradient orientation angles p.d.f.(ϑ) plotted to reveal the underlying structure. Here, ϑ is measured from the downstream axis, so the higher values near $\pm\frac{1}{2}\pi$ directions correspond to layers oriented in the downstream direction (i.e. with their normal vector pointing in the radial direction). If the scalar gradient were isotropically oriented the distribution would be flat with a value of $1/(2\pi)$.

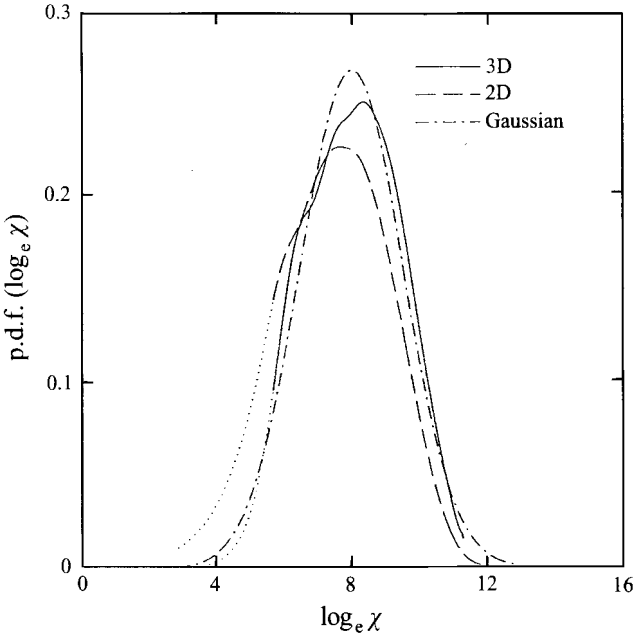

FIGURE 20. The three-dimensional p.d.f. of scalar dissipation rates obtained from the two-dimensional distributions (shown in figure 19) by the technique described by Dahm & Buch (1989). A Gaussian fit to the three-dimensional distributions is plotted for comparison.

amplitudes. These artifacts are the result of any discrete differential operator, like that in (4.10), being applied to the discrete 8-bit data and producing a finite and discrete set of possible azimuth angles. Accordingly, the locations, and even the relative amplitudes, of these spikes are consistent from one measurement to another. It is worth pointing out that the high degree of symmetry in figure 19 is at least partly a quantitative manifestation of the sheet-like fine-scale structure seen in the dissipation fields in §5. Since the dissipation field appears to consist essentially of locally one-dimensional layers with a symmetric internal structure, for every appearance of a $\nabla\zeta(x, t)$ with any particular value of ϑ there will be a reflection through π on the opposite side of the sheet. This reflection will produce a p.d.f. displaying a period-π symmetry in every detail.

Ignoring for the moment the discrete character of the distributions in figure 19, if the underlying $\nabla\zeta(x, t)$ field were fully isotropic then the distribution of ϑ-values should appear uniform. Notice that the results obtained in figure 19(*b*) are, in fact, largely independent of ϑ, although an underlying small and roughly sinusoidal variation with maxima at approximately $\pm\frac{1}{2}\pi$ is discernible. This distribution corresponds to a very slight degree of anisotropy associated with a weak tendency for the dissipation layers to assume a preferred orientation relative to the principal strain axes of the mean flow. In particular, the mean flow has its principal compressive strain axis lying along $\vartheta = \frac{1}{2}\pi$, with a small departure from this value due to the slow growth rate of the flow. Figure 19(*b*) shows that, whereas the scalar gradient field is very nearly isotropic, the gradient vector shows a slight preference to align with this most compressive strain axis. Based on the dynamics in (2.4), as well as classical arguments (e.g. Batchelor 1959), this orientation is to be expected relative to the instantaneous principal strain axes. The consequences of this are discussed in §7.

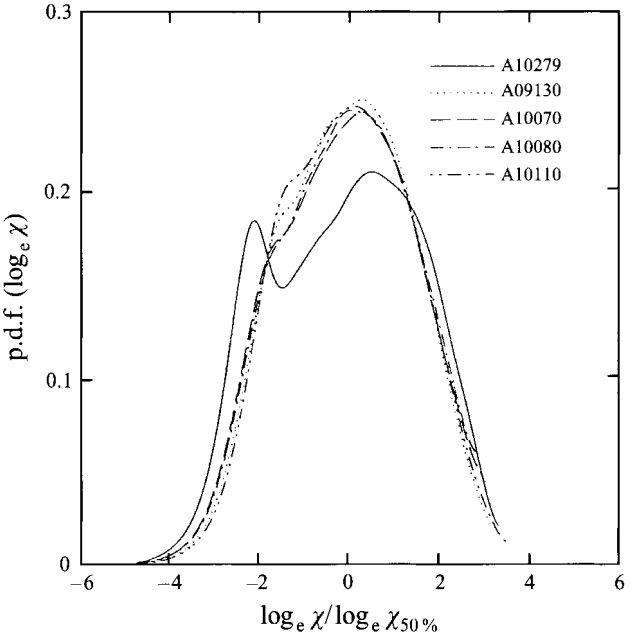

FIGURE 21. Normalized distributions of the logarithm of the three-dimensional scalar dissipation rate.

6.4. *Three-dimensional dissipation distributions*

While it is fundamentally impossible to obtain the true instantaneous local scalar dissipation rate at any single point in the data volume from measurements spanning only two of the three spatial dimensions, it is noteworthy that the distribution of true dissipation rates can nevertheless be exactly obtained from such lower-dimensional measurements using the technique outlined by Dahm & Buch (1989) under the assumption of a known $\beta(\vartheta,\varphi)$. If, on the basis of results such as those in figure 21, the assumption of isotropy in the scalar gradient field is accepted, then the requisite p.d.f. is given by (6.3). Briefly, the central ideal is that each infinitesimal range of true χ-values will produce a distribution of two-dimensional estimates of χ corresponding to a given distribution of true scalar gradient vector orientations. The set of these distributions corresponding to each range of true χ-values forms a linearly independent basis set, and thus the measured p.d.f. can be decomposed into the basis set and the true p.d.f.(χ) reconstructed from the set of delta functions weighted by the corresponding linear coefficients. Numerically, this can be implemented as a marching procedure that starts from the high end of p.d.f.(χ) and incrementally accounts for the area due to each small range of true χ-values.

The solid line in figure 20 shows the three-dimensional dissipation p.d.f. obtained by applying the above procedure to the measured two-dimensional distribution shown in figure 18. The dotted lines correspond to extrapolations of the linear distributions to $\chi = 0$. Also shown for comparison is the Gaussian curve for a precisely log-normal distribution having the same mean and variance as the three-dimensional result. Note that the correction removes much of the asymmetry seen in the two-dimensional distribution, but there is still a clear departure from log-normality.

Figure 21 compares the corrected scalar dissipations p.d.f.s for each data volume. Note that, except for case A10279, all of the results collapse to a single and presumably

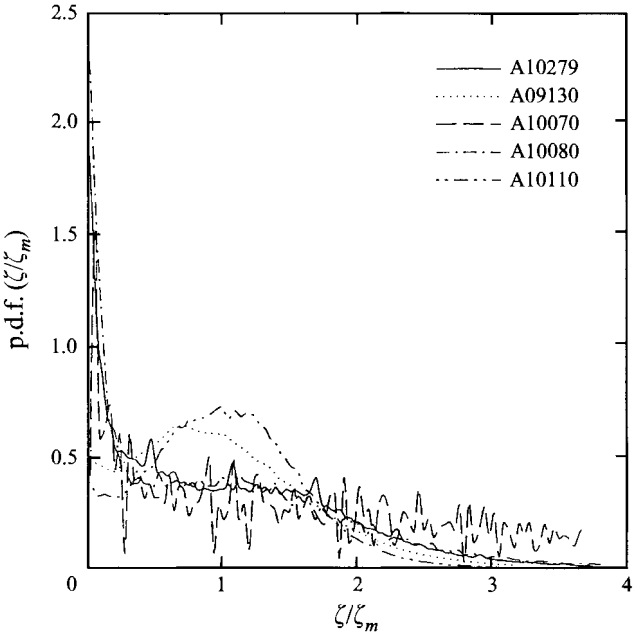

FIGURE 22. Distributions of conserved scalar values ζ normalized by the measured mean value ζ_m.

universal distribution of true scalar dissipation rates. The one case which does not agree is that for which $\Delta T \approx \lambda_D/U$, as indicated in table 2. In that case, the relative time over which the data were collected was presumably too short for the statistics to converge. The departures from log-normality of the dissipation rate distributions apparent in figure 21 are, of course, directly connected with various statistical intermittency models of the type referred to in §2.2, and can be equivalently cast in terms of structure function exponents and the like. Here our interest is focused on noting that, despite the relatively low values of the Reynolds numbers, the dissipation distributions appear to have attained a largely Reynolds-number-independent form, further suggesting that the structure of the dissipation rate fields in figures 7–13 will change only little with increase in Re_δ.

6.5. *Joint probability densities*

Figure 22 shows the measured probability densities of the conserved scalar ζ normalized by the measured mean value ζ_m. While the range of ζ-values collapses fairly well, the shape of the p.d.f.s clearly differs somewhat among these cases. Much of this appears attributable to the rather wide range of dimensionless downstream locations (x/ϑ) represented by the cases shown (see table 1), since the shape of the p.d.f. changes as the flow undergoes the transition from jet-like similarity to wake-like similarity with increasing x/ϑ. Indeed, there is a good correlation evident with x/ϑ for all the cases having fully converged statistics (i.e. all except for A10279). However, at least some of the deviations may also be partly due to the comparatively larger uncertainty in the scalar field values than in the dissipation field values, owing to the beam attenuation effects discussed in §4.1.

Of further interest beyond the individual probability densities p.d.f.(ζ) and p.d.f.(χ), and especially in the modelling of turbulent reacting flows, is the joint distribution of conserved scalar and scalar dissipation, p.d.f.(ζ, χ). Since the scalar and dissipation rate values are known simultaneously at every point in each data volume,

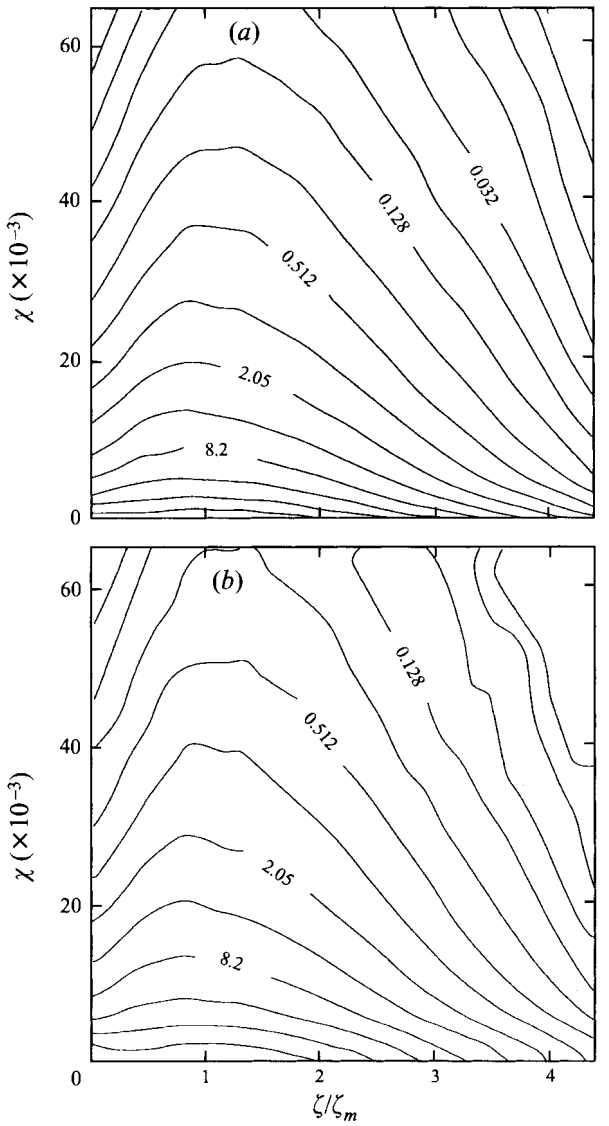

FIGURE 23. (*a*) The joint distribution of conserved scalar values and two-dimensional scalar dissipation rates for data set A09130. (*b*) The joint distribution of conserved scalar values and three-dimensional scalar dissipation rates calculated from the distribution in (*a*).

the joint distributions can be readily constructed. Figure 23(*a*) shows a typical result for the joint distribution p.d.f.(ζ, χ), corresponding to case A09130, shown in figures 8–10. Notice that, owing to the wide range of dissipation rates encountered, the contour levels shown increase logarithimically, with adjacent contours differing by factors of two. This distribution was computed using the measured two-component values of the scalar dissipation rate, and suggests that the scalar and dissipation values are largely statistically independent, namely p.d.f.(ζ, χ) ~ p.d.f.(ζ)p.d.f.(χ). Each conditional two-dimensional scalar dissipation p.d.f. obtained from the joint distribution shown can be converted to the corresponding true, three-dimensional condition distribution following the procedure outlined in §6.4. These marginal distributions can then be combined to produce the true three-dimensional joint

$$\int_E \left(\frac{\partial \Gamma}{\partial t}\right)_{v^1,v^2} \mathrm{d}S = \int_E \boldsymbol{w}\cdot\boldsymbol{\nabla}_s\Gamma\,\mathrm{d}S - \int_C \Gamma \boldsymbol{u}_s\cdot\boldsymbol{b}\,\mathrm{d}l - 2\int_E \Gamma\kappa_m \boldsymbol{u}\cdot\boldsymbol{n}\,\mathrm{d}S + D_s\int_C \boldsymbol{b}\cdot\boldsymbol{\nabla}_s\Gamma\,\mathrm{d}l, \tag{A 7}$$

where $\mathrm{d}S$ and $\mathrm{d}l$ are, respectively, the differential surface area of E and the differential arclength along C. We have introduced the unit vector $\boldsymbol{b} = \boldsymbol{t}\times\boldsymbol{n}$, where $\boldsymbol{t}$ is the unit vector that is tangential to C and points in the counterclockwise direction when the interface is observed from the outside, as depicted in figure 18(*a*). The implementation of the finite-volume method for solving (A 7) over the triangulated interface of a deforming drop is discussed by Yon & Pozrikidis (1998).

A.2. *Axisymmetric interfaces*

The surfactant concentration evolution equation for an axisymmetric interface follows readily by considering the trace of the interface in the (x,y) azimuthal plane denoted as C, labelling marker points distributed along C with the curvilinear coordinate v^1, and identifying v^2 with the azimuthal angle φ, as shown in figure 18(*b*).

To develop the finite-volume formulation, we introduce the unit vector $\boldsymbol{t}$ that is tangential to C and points in the direction of increasing v^1, denote the corresponding arclength as l, and consider an interfacial element E with endpoints A and B, as shown in figure 18(*b*). Performing the integration in the azimuthal direction analytically, we find that equation (A 7) reduces to

$$\int_E \left(\frac{\partial \Gamma}{\partial t}\right)_{v^1} \sigma\,\mathrm{d}l = \int_E \boldsymbol{w}\cdot\boldsymbol{t}\frac{\partial \Gamma}{\partial l}\sigma\,\mathrm{d}l - (\Gamma\sigma\boldsymbol{u}\cdot\boldsymbol{t})_B + (\Gamma\sigma\boldsymbol{u}\cdot\boldsymbol{t})_A$$
$$- \int_E \Gamma\kappa\boldsymbol{u}\cdot\boldsymbol{n}\sigma\,\mathrm{d}l + D_s\left(\sigma\frac{\partial \Gamma}{\partial l}\right)_B - D_s\left(\sigma\frac{\partial \Gamma}{\partial l}\right)_A. \tag{A 8}$$

This equation is the starting point for the numerical procedure discussed in §2.

A.3. *Two-dimensional interfaces*

The differential form of the surfactant concentration evolution equation for a two-dimensional interface in the (x,y)-plane follows readily after a straightforward change in notation. In this case, the marker points are labelled using the single curvilinear coordinate v^1, as shown in figure 18(*c*).

To implement the finite-volume formulation, we introduce the tangential unit vector along the interface $\boldsymbol{t}$, pointing in the direction of increasing v^1, denote the corresponding arclength by l, and consider an interfacial element E with end points A and B, as shown in figure 18(*c*). The counterpart of (A 7) is

$$\int_E \left(\frac{\partial \Gamma}{\partial t}\right)_{v^1} \mathrm{d}l = \int_E \boldsymbol{w}\cdot\boldsymbol{t}\frac{\partial \Gamma}{\partial l}\,\mathrm{d}l - (\Gamma\boldsymbol{u}\cdot\boldsymbol{t})_B + (\Gamma\boldsymbol{u}\cdot\boldsymbol{t})_A$$
$$- \int_E \Gamma\kappa\boldsymbol{u}\cdot\boldsymbol{n}\,\mathrm{d}l + D_s\left(\frac{\partial \Gamma}{\partial l}\right)_B - D_s\left(\frac{\partial \Gamma}{\partial l}\right)_A, \tag{A 9}$$

where κ is the curvature of the trace of the interface in the (x,y)-plane. This equation is the starting point for the numerical procedure discussed in §2.

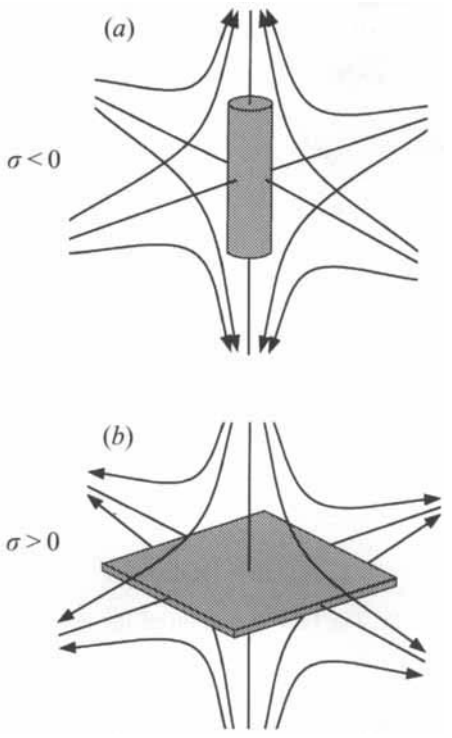

FIGURE 25. The two classes of local strain rate structures possible in a flow field where the coordinate frame remains aligned with the local instantaneous principal axes of the strain rate tensor: (*a*) $\sigma < 0$ and (*b*) $\sigma > 0$.

essentially all the dissipation is concentrated, and having quantified various statistical features associated with these dissipation fields in §6, we now examine the internal structure of these scalar dissipation layers. We first review several features of the canonical solutions for the strain–diffusion balance that leads to the formation of these dissipation layers. Following this, in §7.4, we compare measurements of the internal structure of these layers with these simple idealized representations.

7.1. *Characterization of the local strain rate field*

Viewing the local velocity field in a translating and rotating coordinate frame moving with any chosen material point in the flow, and remaining aligned with the local instantaneous principal axes of the strain rate tensor $\boldsymbol{\epsilon} = \frac{1}{2}(\boldsymbol{\nabla u} + \boldsymbol{\nabla u}^T)$, the local strain rate tensor can be represented by its principal strain rates $\epsilon_{11} \geqslant \epsilon_{22} \geqslant \epsilon_{33}$ as

$$\boldsymbol{\epsilon} = (\epsilon_{11}, \epsilon_{22}, \epsilon_{33}). \tag{7.1}$$

Continuity requiring $\epsilon_{11}+\epsilon_{22}+\epsilon_{33} = 0$ in turn requires $\epsilon_{11} \geqslant 0$ and $\epsilon_{33} \leqslant 0$, thus the strain rate tensor in (7.1) can be equivalently written as

$$\boldsymbol{\epsilon} = \epsilon_{11}(1, \sigma, -(1+\sigma)), \tag{7.2}$$

where $\sigma \equiv \epsilon_{22}/\epsilon_{11}$ is a single parameter describing the structure of the local strain rate tensor, and ϵ_{11} simply characterizes the magnitude of the principal strain rate components. The latter serves only to rescale time in the local dynamics. As for the former, this structure parameter is bounded by $-\frac{1}{2} \leqslant \sigma \leqslant 1$, so two classes of local strain rate fields are possible, as shown in figure 25. The first, namely $\sigma > 0$, corresponds to two extensional and one compressional principal strain axes. Local

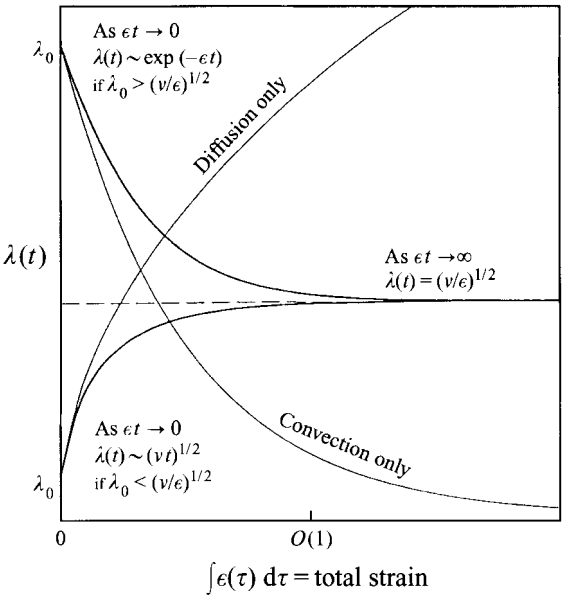

FIGURE 26. The time evolution of the lengthscale λ_ν.

kinematic considerations (i.e. (2.4) and (2.5)) show that the deformations produced when $\sigma > 0$ will distort any material volume toward a sheet-like topology whose local gradient $\nabla\zeta$ will tend to align with the eigenvector for the most compressive principal strain rate ϵ_{11}, as shown in figure 25(*b*). On the other hand, when $\sigma < 0$ the local flow tends to deform a material volume into a line-like topology as indicated in figure 25(*a*), with $\nabla\zeta$ again tending to rotate toward the most compressive principal strain rate axis. Taking non-inertial effects to be negligible, exact local solutions of (2.1) and (2.2) are possible for limiting cases including $\sigma = -\frac{1}{2}$, 0, and 1, corresponding to locally axisymmetric and planar strain rate fields. These solutions produce the sheet-like and line-like topologies described by Burgers (1948, 1950) and Townsend (1951). A discussion of these strain-limited solutions for vortex 'sheets' and 'lines' in steady strain fields is given by Sherman (1990, pp. 155–156 and 564–567); see also Batchelor (1967, pp. 271–273). The extension to time-varying strain fields is given by Carrier, Fendell & Marble (1975, equations (4.1)–(4.4)). Here we also examine solutions and their implications for the local conserved scalar field structure and dynamics.

7.2. *Formation of line-like dissipative structures* ($\sigma = -\frac{1}{2}$)

For $\sigma = -\frac{1}{2}$, the extensionally strained vorticity component and conserved scalar must satisfy

$$\frac{\partial\omega}{\partial t} + (-\epsilon_{11} r)\frac{\partial\omega}{\partial r} - \nu\left(\frac{\partial^2\omega}{\partial r^2} + \frac{1}{r}\frac{\partial\omega}{\partial r}\right) = 2\epsilon_{11}\omega, \tag{7.3a}$$

$$\frac{\partial\zeta}{\partial t} + (-\epsilon_{11} r)\frac{\partial\zeta}{\partial r} - D\left(\frac{\partial^2\zeta}{\partial r^2} + \frac{1}{r}\frac{\partial\zeta}{\partial r}\right) = 0. \tag{7.3b}$$

Self-similar solutions of the form

$$\omega(r,t) = \frac{\Gamma}{\lambda^2(t)} f(\eta), \quad \zeta(r,t) = \zeta_m(t)\, g(\eta\, Sc^{1/2}), \tag{7.4a, b}$$

where

$$\eta \equiv r/\lambda(t), \tag{7.5}$$

demand

$$\lambda^2(t) = \exp\left(-\int_0^t 2\epsilon_{11}(t')\,\mathrm{d}t'\right)\left[\lambda_0^2 + 2\nu\int_0^t \exp\int_0^{t'} 2\epsilon_{11}(t'')\,\mathrm{d}t''\,\mathrm{d}t'\right]. \tag{7.6}$$

The result in (7.4) and (7.6) for the time evolution of the lengthscale $\lambda(t)$ characteristic of the local gradient scales in the vorticity and conserved scalar fields is shown in figure 26. In particular, notice that regardless of the initial gradient lengthscale λ_0, at large times the competing effects of strain and diffusion reach an equilibrium at the strain-limited diffusion lengthscale $\lambda_\nu \sim (\nu/\epsilon_{11})^{1/2}$, where the gradient scale λ no longer changes explicitly with time, and instead is set by the strain rate ϵ_{11}. Furthermore, note that the response of these fields to a subsequent change in strain rate is a strain-imposed exponential decrease toward the new diffusion-limited equilibrium scale λ_ν on a timescale set by ϵ_{11} if the initial lengthscale $\lambda_0 > \lambda_\nu$, or conversely a diffusion-dominated square-root increase toward this same strain-limited equilibrium scale if $\lambda_0 < \lambda_\nu$. Except for a short time of $O(1/\epsilon_{11})$, the Lagrangian strain history is unimportant in setting the diffusion scale. Instead, the gradient lengthscale is largely dominated by the local strain–diffusion competition.

When ϵ_{11} is of the order of the local outer-scale strain rate (u/δ), this equilibrium lengthscale becomes $(\lambda_\nu/\delta) \sim Re_\delta^{-1/2}$ and corresponds to the local Taylor scale. On the other hand, when ϵ_{11} is of the order of the local inner-scale strain rate $(u/\delta)\,Re_\delta^{1/2}$, the equilibrium lengthscale in (7.6) becomes $(\lambda_\nu/\delta) \sim Re_\delta^{-3/4}$ and corresponds to the local Kolmogorov scale.

The invariance in the circulation Γ of the resulting line-like vortical structure demands a Gaussian core for the vorticity in (7.4*a*) of the form

$$\omega(\eta, t) = \frac{1}{2\pi}\frac{\Gamma}{\lambda^2(t)}\exp(-\tfrac{1}{2}\eta^2). \tag{7.7}$$

Self-similarity demands that the centreline conserved scalar value $\zeta_m(t)$ in (7.4*b*) must decay exponentially with time as

$$\zeta_m \to \exp -2\int_0^t \epsilon_{11}(t')\,\mathrm{d}t'. \tag{7.8}$$

This can be understood directly from conservation of the total amount of scalar, and demonstrates that, while such line-like structures can be indefinitely sustained in the vorticity field, no similar line-like structures can be maintained in the conserved scalar gradient field. As mentioned in §2.2, results from direct numerical simulations routinely show line-like structures in the vorticity field, while the results in figures 7–13 show no evidence of such line-like structures in the scalar dissipation field.

7.3. *Formation of sheet-like dissipative structures* ($\sigma = 0$)

For $\sigma = 0$ and 1, (2.1) takes the form

$$\frac{\partial\zeta}{\partial t} + (-\epsilon_{11}n)\frac{\partial\zeta}{\partial n} - D\frac{\partial^2\zeta}{\partial n^2} = 0. \tag{7.9}$$

Self-similar solutions analogous to (7.4*a*, *b*) demand that the gradient lengthscale $\lambda(t)$ in both the vorticity and scalar gradient fields must again satisfy (7.6) as in figure 26.

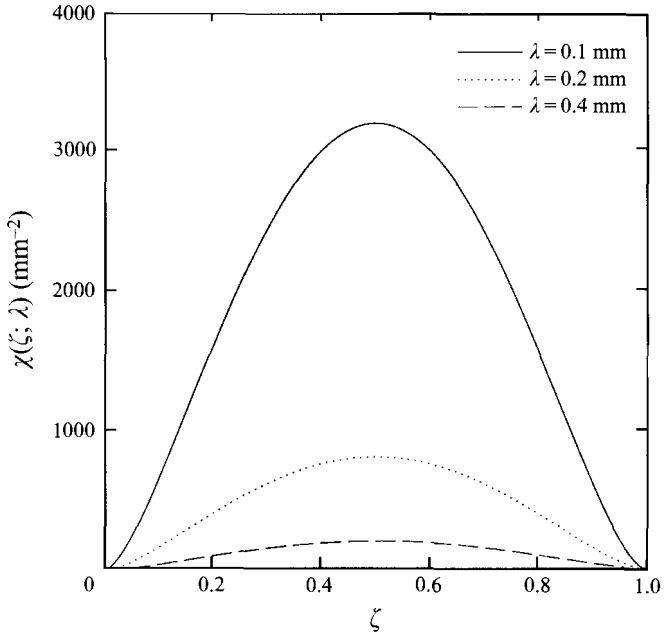

FIGURE 27. The variation in scalar dissipation with conserved scalar, $\chi(\zeta)$, from (7.14) with $(\zeta^+, \zeta^-) = (0, 1)$ for three different layer thicknesses λ_D. Compare with the general form the joint p.d.f. $\beta(\zeta, \chi)$ in figure 26.

In this case, sheet-like structures can be indefinitely sustained in both the vorticity and scalar gradient fields. In the latter, two solutions are possible. The first corresponds to a scalar gradient region between two equal scalar boundary values ζ^+ and ζ^-, but the extremum scalar value must again decay exponentially as given in (7.8). The other case corresponds to a gradient sheet between two different scalar boundary values $\zeta^+ \neq \zeta^-$. In this case, $\zeta_m(t) = \frac{1}{2}(\zeta^+ + \zeta^-)$ remains constant in time and the scalar field has an error-function profile along the local sheet-normal coordinate n given by

$$\zeta(n, t) = \tfrac{1}{2}(\zeta^+ + \zeta^-) + \tfrac{1}{2}(\zeta^+ - \zeta^-)\,\mathrm{erf}\left(\frac{n}{\lambda_D(t)}\right), \tag{7.10a}$$

$$\lambda_D(t) = \lambda(t)\, Sc^{-1/2}, \tag{7.10b}$$

where $\mathrm{erf}(\xi)$ is the error function

$$\mathrm{erf}(\xi) \equiv \frac{2}{\pi^{1/2}} \int_0^{\xi} \exp(-\eta^2)\, \mathrm{d}\eta. \tag{7.11}$$

For an isolated sheet-like scalar gradient structure of the type described by (7.6) and (7.10), the corresponding scalar dissipation profile across the layer will be Gaussian, given by

$$\nabla\zeta \cdot \nabla\zeta(n, t) = \frac{1}{\pi}\left[\frac{(\zeta^+ - \zeta^-)}{\lambda_D(t)}\right]^2 \exp\left\{-2\left(\frac{n}{\lambda_D(t)}\right)^2\right\}. \tag{7.12}$$

Accordingly, the logarithm of the scalar dissipation will have an inverted parabolic profile of the form

$$\log_e\{\nabla\zeta \cdot \nabla\zeta(n, t)\} = -2\left(\frac{n}{\lambda_D(t)}\right)^2 + 2\log_e\left\{\frac{1}{\pi}\left[\frac{(\zeta^+ - \zeta^-)}{\lambda_D(t)}\right]\right\}. \tag{7.13}$$

From (7.10) and (7.12), the corresponding expression for $\chi(\zeta;\zeta^{\pm},\lambda)$ is simply

$$\chi(\zeta;\zeta^{\pm},\lambda)=\frac{D}{\pi}\left[\frac{(\zeta^{+}-\zeta^{-})}{\lambda_D(t)}\right]^2\exp\left\{-2\left[\mathrm{erf}^{-1}\left(\frac{\zeta-\frac{1}{2}(\zeta^{+}+\zeta^{-})}{\frac{1}{2}(\zeta^{+}-\zeta^{-})}\right)\right]^2\right\}, \tag{7.14}$$

where $\mathrm{erf}^{-1}(\xi)$ is the inverse error function. Note that in (7.14) the characteristic gradient lengthscale λ_D acts only as a scaling constant, producing a family of curves that are all self-similar and scale as λ_D^{-2}. Furthermore, in the equilibrium limit, where $\lambda\sim(D/\epsilon)^{1/2}$, the scalar dissipation scales linearly with the strain rate ϵ. This function $\chi(\zeta;\lambda)$ is shown in figure 27 for $(\zeta^{+},\zeta^{-})=(1,0)$ and three different values of λ_D corresponding, in the equilibrium limit, to three different values of the strain rate ϵ.

Figure 27 gives an idea of the shape of the joint probability density function for the ideal canonical scalar interface and corresponding dissipation layers. The λ^{-2} scaling produces a family of curves that rapidly decrease in amplitude as λ increases. Since the scalar value has a higher probability of being near the endpoints ζ^{+} and ζ^{-}, the p.d.f. will have larger values near those values which correspond to χ near zero. Therefore, the resulting joint p.d.f. will have contours that become more dense as χ approaches zero. A comparison of this description with the joint p.d.f.s computed in §6.5 shows a strong qualitative agreement, supporting the assumption that the dissipation field can be modelled in terms of the canonical sheet-like dissipation structure.

7.4. *Comparisons with measurements*

Representative examples of the internal structure in the measured scalar and dissipation fields are presented in figure 28. These are enlarged views of fields such as those presented in §5, showing the shape of the respective profiles along an intersection through a scalar interface. Since gradients in the strain rate and vorticity occur over regions of $O(Sc^{1/2})$ larger than λ_D, at large Schmidt numbers the strain field experienced by two adjacent interacting scalar gradient layers will be nearly the same. Therefore, their thicknesses should be nearly the same and they should be nearly parallel.

Qualitative comparisons can be made in figure 28 with the error-function profile for the scalar field in (7.10), the Gaussian profile for the dissipation field in (7.12), and the parabolic profile for the logarithm of the dissipation field in (7.13). A qualitative and more objective numerical comparison, that covers most of the layers in these planes, can also be made. The first four moments of the layer-normal profiles were used to characterize their internal structure, from which we examine the skewness S and the kurtosis K corresponding to the internal layer structure. Each profile was clipped beyond the points where the scalar dissipation dropped below 20% of the peak value in the layer, and renormalized to unity area before computing the moments. For a Gaussian profile clipped in this manner, the skewness is zero and the kurtosis is 2.26. Moments of order higher than 4 were not examined, since these increasingly emphasize the structure in the tails of the profile, where the dissipation becomes small and interactions with neighbouring layers become significant.

Figure 29(*a*) shows the distribution of skewness values obtained for varying numbers of data planes. Note that, since each data plane typically contains at least a few hundred layer profiles, the statistics from just a few temporally uncorrelated data planes converge rapidly. The strong peak near zero in figure 29(*a*) demonstrates that in general the layer are at least roughly symmetric about their mean. Figure 29(*b*) shows the distributions of kurtosis values for the same layers as in figure 29(*a*). Note the strong peak near the value of 2.26, suggesting that at least the central portion of the dissipation profiles is typically in good agreement with the simple canonical pictures described above.

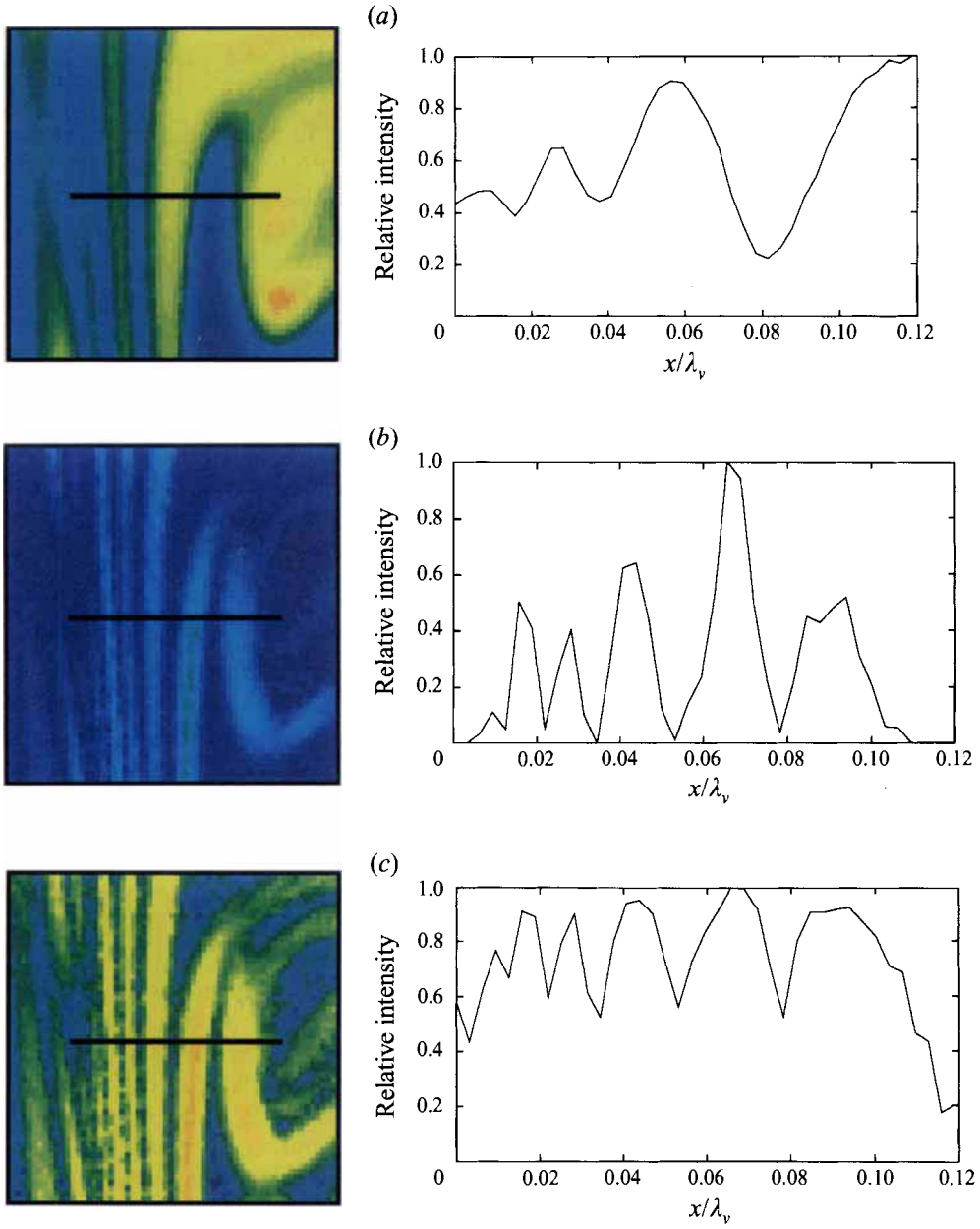

FIGURE 28. Profile through a scalar interface in (*a*) the conserved scalar field, (*b*) the scalar dissipation rate field and (*c*) the logarithm of the scalar dissipation rate field.

If, on the basis of results such as those above, the scalar dissipation fields can be modelled as being composed entirely of isolated sheet-like strained laminar diffusion layers of the type in §7.3 between scalar values (ζ^+, ζ^-), then the distribution of scalar dissipation rates would be completely determined by just three parameters describing these layers. As noted in Appendix B, these parameters are the maximum dissipation value in the layer, the layer thickness, and the radius of curvature of the layer. Here, we only include the effect of layer maximum value, and from this compute a theoretical

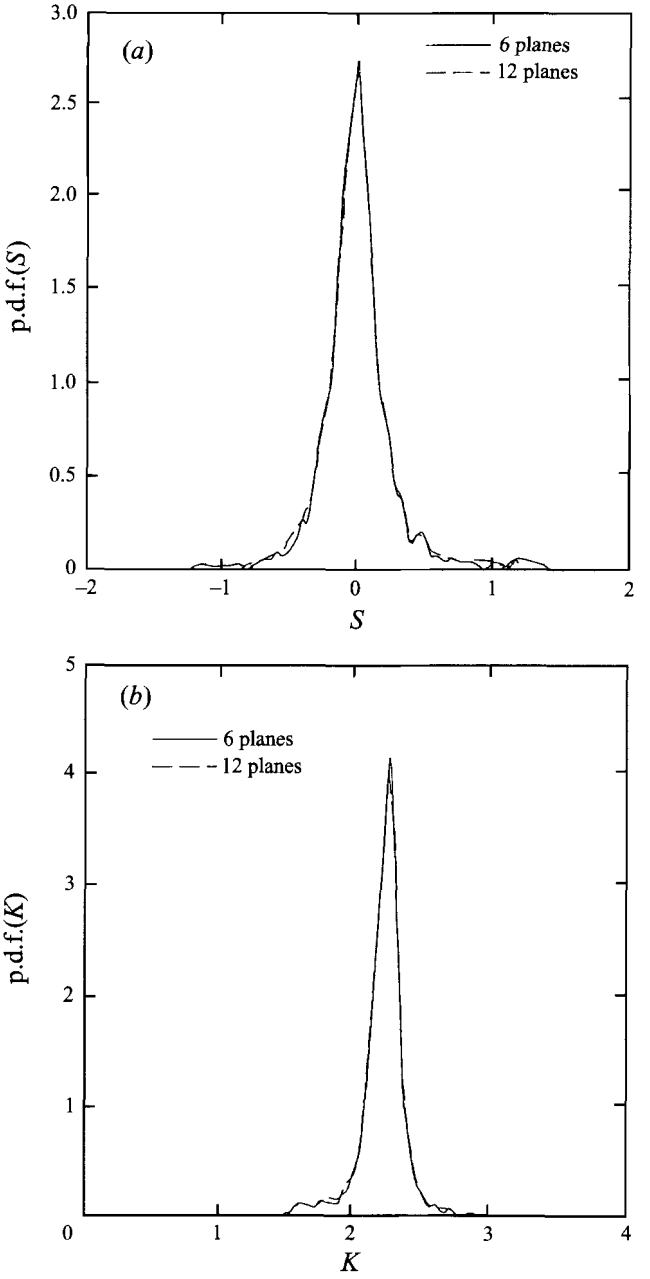

FIGURE 29. (*a*) Distributions of skewness values of profiles through molecular diffusion layers. For a layer with a Guassian profile, the skewness is 0 since the profile is symmetric. (*b*) Distributions of kurtosis values of profiles through molecular diffusion layers. A Gaussian profile that has been clipped at the 20% point and renormalized has a kurtosis of 2.26.

dissipation distribution. Figure 30 shows the distribution of the local maximum dissipation rate within the dissipation layers. Using this distribution and the procedure in Appendix B, the theoretical scalar dissipation rate distribution is shown in figure 31. Note the excellent agreement at the higher values of χ. The discrepancies at the lower values are, at least in part, likely to result from interactions between layers and the fact that $\zeta^{\pm}$ differ from (0, 1).

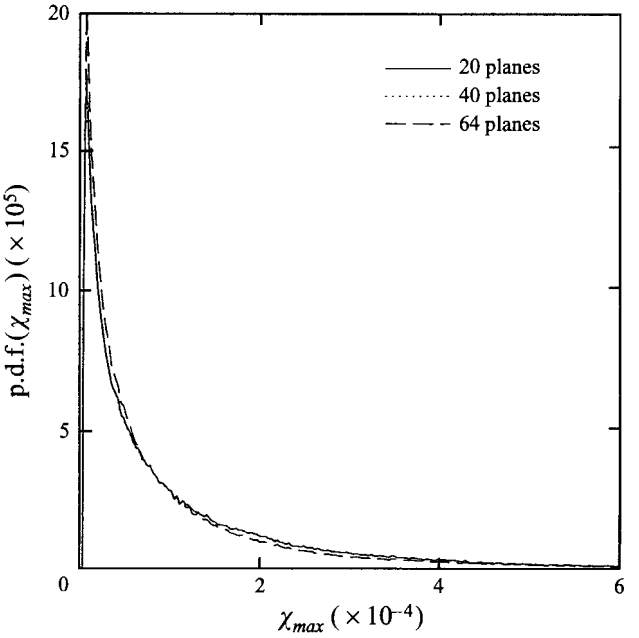

FIGURE 30. Distributions of layer maxima for the molecular diffusion layers.

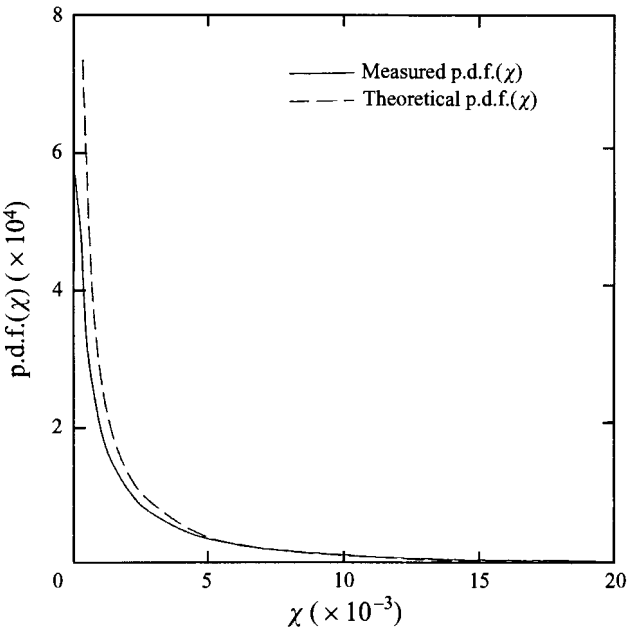

FIGURE 31. A comparison of the measured distribution of scalar dissipation rates and the predicted distribution obtained from the measured distribution of molecular diffusion layer maximum.

8. Discussion and conclusions

The results presented from this study offer detailed views the fine-scale structure of $Sc \gg 1$ conserved scalar mixing in turbulent flows. These experimental measurements have yielded highly resolved data on the conserved scalar and scalar gradient fields,

which are not accessible to direct numerical simulations owing to the large Sc involved. The data provide a physical picture of the scalar field fine structure on the local inner scale of the flow. The outer-scale Reynolds numbers Re_δ in these experiments are believed to be high enough that at least the basic structure of the scalar dissipation field has attained its asymptotic high Reynolds number form. However, it seems unlikely that these Reynolds numbers are high enough for all of the details associated with this fine structure to have reached a strictly Reynolds-number-independent form. In this sense, the fine structure seen in these data is viewed as giving a correct indication of the high Reynolds number asymptotic state of turbulent mixing, but at least some quantitative details of the mixing process will likely still depend on the outer-scale Reynolds number. Evidence of this can be found in the fact that there does not appear to be any fundamental change in topology of the scalar dissipation fields, when viewed on inner variables, over the range of Reynolds numbers investigated, as well as in the similarity demonstrated on inner-scale variables by the various statistical quantities examined.

Perhaps most noteworthy are the observations in §5 of a manifestly sheet-like topology in the scalar dissipation rate field that underlies the $Sc \gg 1$ mixing process at the small scales of turbulent flows. Unlike the vorticity field in turbulent flows, the scalar gradients are concentrated solely on sheet-like small-scale structures. The fine structure in the scalar gradient field is thus far simpler than that in the vorticity field. The apparent reason for this more restricted range of topologies in the scalar gradient field in comparison with the vorticity field was examined in §7 and can be traced to the dynamics summarized in §2.1. In effect, line-like structures in the scalar dissipation field must decay exponentially in time, but can be sustained indefinitely in the vorticity. Both fields can however sustain sheet-like structures. Thus as the local $\sigma(t)$ in (7.2) changes, the vorticity field presumably undergoes a continual tendency to evolve between locally sheet-like and line-like topologies, whereas the scalar dissipation dynamics allow only the sheet-like structures to be sustained. Note that the insights into the fine structure of the scalar mixing in turbulent flows provided by these data also supports the fluid dynamic foundations of certain sheet-like conceptual models of reacting turbulent flows, such as the 'flamelet' models by Gibson & Libby (1972), Liew, Bray & Moss (1981), Peters & Williams (1983), Peters (1984), and Pope & Cheng (1988).

A further point of interest which can be seen in figures 7–13 is the topology associated not only with the fundamental sheet-like structure of the individual dissipation layers themselves, but also the arrangement of these layers relative to one another. In particular, these figures show highly convoluted patterns into which the dissipation layers are kneaded by the continual stretching action of the strain field, the folding action due to differential rotations introduced by gradients in the vorticity field, and the continuous reorientation of the local principal strain rate axes. Among the range of dissipation layer patterns, several fundamental topologies can be identified. These include (i) long regions consisting of many straight and nearly parallel dissipation layers, (ii) areas where two such long regions meet nearly orthogonally, identifiable for example in figures 9(*c*) and 11(*b*) where the dissipation layers adopt a pattern somewhat reminiscent of the streamlines in the classical stagnation point flow, and (iii) regions where the dissipation layers form a set of roughly concentric curved sheets suggestive of scalar interfaces wrapped around line-like vortical structures as seen in Kerr (1985). These topologies have a strong resemblance to the phase portraits in critical point theory (e.g. Ottino 1982, 1989), namely the simple shear, saddle, and centre (or whorl) portraits. While an analysis of these data in terms

of fixed and periodic points may be possible, for the present purpose we simply note that practically the entire dissipation field is composed of relatively few patterns, and this suggests possibilities for modelling the mixing process on these larger scales.

Finally, it is noteworthy that both the sheet-like topology of the dissipation field and the large-scale arrangement of the dissipation layers are, at least qualitatively, similar to results obtained by Ottino (1982, 1989) for chaotic advection in asymptotically low Reynolds number flows. In that case, the continual reorientation of the principal strain axes leads to the formation of 'striations' in the scalar field that strongly resemble many of the features seen in the present turbulent flow data. Indeed, the key component in both cases appears to be the stretching and folding induced by the time-varying velocity gradient field. The overall similarity between these two flows suggests a degree of universality at the small scales that may extend across the Reynolds number boundaries traditionally associated with low Reynolds number chaotic mixing and the much higher Reynolds numbers in the turbulent flows examined here.

Appendix A. Uncertainty estimates for scalar dissipation data

From the discrete template in (4.9), the values $\chi(\boldsymbol{x}_i, t)$ in the scalar energy dissipation rate field can be expressed in terms of the measured scalar field values $\zeta(\boldsymbol{x}_j, t)$ as

$$\chi = \chi_A^2 + \chi_B^2, \tag{A 1}$$

where

$$\chi_A \equiv \chi_{A_1} + \chi_{A_2}, \quad \chi_B \equiv \chi_{B_1} + \chi_{B_2}, \tag{A 2a, b}$$

with

$$\chi_{A_1} \equiv \left(\frac{1}{4\Delta}\right)(\zeta_1 - \zeta_2), \quad \chi_{B_1} \equiv \left(\frac{1}{4\Delta}\right)(\zeta_7 - \zeta_8), \tag{A 3a, b}$$

and

$$\chi_{A_2} \equiv \left(\frac{1}{8\Delta}\right)(\zeta_3 + \zeta_4 - \zeta_5 - \zeta_6), \quad \chi_{B_2} \equiv \left(\frac{1}{8\Delta}\right)(\zeta_3 + \zeta_6 - \zeta_5 - \zeta_4) \tag{A 4a, b}$$

and where ζ_1 to ζ_8 denote the eight pixels surrounding any given pixel in any data plane.

Denoting the uncertainty in the measured scalar field values as σ_ζ, it is possible to quantify the uncertainty σ_χ that results in the dissipation values using standard statistical methods (e.g. Bevington 1969). Note that for constants (a, b) and variables (u, v), if

$$p \equiv au \pm bv \quad \text{and} \quad q \equiv au^{\pm b}, \tag{A 5a, b}$$

then the resulting uncertainties in p and q are

$$\sigma_p^2 = a^2\sigma_u^2 + b^2\sigma_v^2 \pm 2ab\sigma_{uv}^2 \quad \text{and} \quad \sigma_q = abu^{\pm b-1}\sigma_u, \tag{A 6a, b}$$

where the variances $\sigma_u^2 \equiv \langle u'^2 \rangle$ denote the uncertainties in each of the variables and the covariances $\sigma_{uv}^2 \equiv \langle u'v' \rangle$ denote the uncertainty correlations between variables. Thus in (A 1) to (A 4), if the noise statistics in all adjacent pixels are the same, then the variances σ_ζ^2 in all the ζ_i will be the same, and if moreover the noise in adjacent pixels is independent then all the covariances will be zero. Consequently

$$\sigma_{\chi_{A_1}}^2 = \sigma_{\chi_{B_1}}^2 = \left(\frac{1}{4\Delta}\right)^2 2\sigma_\zeta^2, \quad \sigma_{\chi_{A_2}}^2 = \sigma_{\chi_{B_2}}^2 = \left(\frac{1}{8\Delta}\right)^2 4\sigma_\zeta^2, \tag{A 7a, b}$$

and

$$\sigma_{\chi_A}^2 = \sigma_{\chi_B}^2 = \left(\frac{1}{4\Delta}\right)^2 2\sigma_\zeta^2 + \left(\frac{1}{8\Delta}\right)^2 4\Delta_\zeta^2. \tag{A 8}$$

Then

$$\sigma_{\chi_A^2} = 2\chi_A \sigma_{\chi_A}, \quad \sigma_{\chi_B^2} = 2\chi_B \sigma_{\chi_B}, \tag{A 9a, b}$$

so finally

$$\sigma_\chi^2 = \sigma_{\chi_A^2}^2 + \sigma_{\chi_B^2}^2 = \tfrac{3}{4}\chi \frac{\sigma_\zeta^2}{\Delta^2}, \tag{A 10}$$

with the resulting fractional error in the dissipation being

$$\left(\frac{\sigma_\chi}{\chi}\right) = \frac{\sqrt{3}}{2}\frac{1}{\sqrt{\chi}}\left(\frac{\sigma_\zeta}{\Delta}\right). \tag{A 11}$$

Normalizing on inner variables as in figures 7–13, where

$$\tilde{\chi} \equiv \frac{\chi}{(\zeta_m/\lambda_\nu)^2} \tag{A 12}$$

gives

$$\left(\frac{\sigma_{\tilde{\chi}}}{\tilde{\chi}}\right) = \frac{\sqrt{3}}{2}\frac{1}{\sqrt{\tilde{\chi}}}\left(\frac{\sigma_\zeta/\zeta_m}{\Delta/\lambda_\nu}\right). \tag{A 13}$$

As noted in §4.4, the r.m.s. camera noise level is approximately 1 digital signal level, whereas the mean scalar value corresponds to approximately 80 levels, and thus $(\sigma_\zeta/\zeta_m) \approx (1/80)$. In table 2 the in-plane pixel spacing Δ is typically 50 μm, and $\lambda_\nu = \lambda_D Sc^{1/2}$ with $Sc \approx 2000$ and λ_D typically 150 μm. With these values, from (A 13) the fractional uncertainty in the normalized dissipation values can be obtained for any dissipation value. At the peak dissipation value of 84000 in figures 7–13 the resulting fractional uncertainty is (1/185), while near the mean value of 6000 the fractional uncertainty is (1/48). These can be compared with the fractional uncertainties of (1/256) at the peak measured scalar values and (1/80) at the mean scalar value.

Appendix B. Scalar dissipation statistics from the distribution of layer maximum values

The scalar dissipation field for $Sc \gg 1$ seen in these measurements is almost entirely organized into thin sheet-like gradient regions. From this and the observation that the internal structure of these sheets is at least approximately Gaussian, it is possible to construct an idealized scalar dissipation distribution from the distribution of local sheet-normal maximum dissipation values.

For a dissipation field composed of such sheets, with arbitrary widths and radii of curvature, the dissipation is zero everywhere except in the sheets, where

$$\chi = \chi_m \exp(-\lambda n^2), \tag{B 1}$$

where χ_m is the layer maximum value, λ is the measure of the thickness of the sheet, and n is the local sheet-normal coordinate. The probability that any measurement of the scalar dissipation rate χ^* is less than some threshold χ can be expressed in terms of the probability of making that measurement at some location in the layer. It can be seen that

$$P(\chi^* < \chi) = P(-n_e < n^* < -n) + P(n < n^* < n_e) \tag{B 2a}$$

$$= \frac{\displaystyle\int_{\theta_1}^{\theta_2} \theta \,\mathrm{d}\theta \int_{-n_e}^{-n} (r-n)\,\mathrm{d}n + \int_{\theta_1}^{\theta_2} \theta \,\mathrm{d}\theta \int_{n}^{n_e} (r-n)\,\mathrm{d}n}{\displaystyle\int_{\theta_1}^{\theta_2} \theta \,\mathrm{d}\theta \int_{-n_e}^{n_e} (r-n)\,\mathrm{d}n} \tag{B 2b}$$

$$= \frac{r(1-n/n_e) - \frac{1}{2}n_e}{r - \frac{1}{2}n_e}, \tag{B 2c}$$

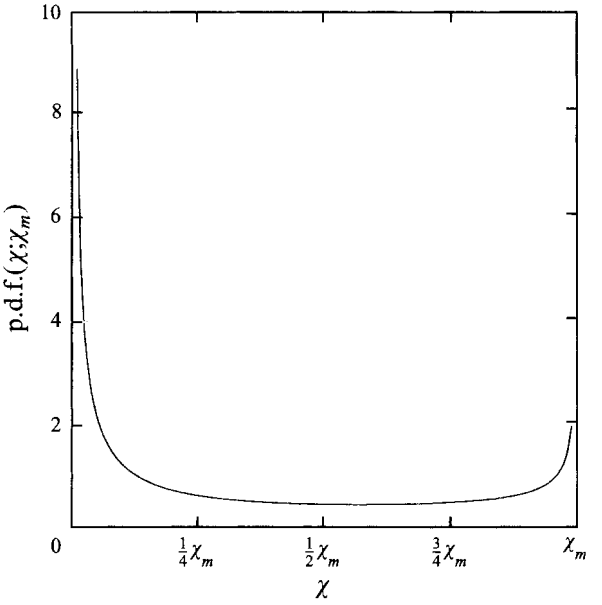

FIGURE 32. Distribution of scalar dissipation rate values from (B 4).

where n_e defines the edge of the layer (where $\chi = \chi_e$ is some fraction of χ_m) and r is the local radius of curvature. The integration over θ would be over that range of angles where the local radius of curvature of the layer is constant; however, this contribution cancels.

Note that (B 2c) contains information about the local layer maximum, the local radius of curvature, and the thickness of the diffusion layers comprising the model scalar dissipation field. While all of these effects could be accounted for by determining the appropriate probability distributions, if it is assumed that the local radius of curvature r is large compared to the width n_e of the layers, then this simplifies to

$$P(\chi^* < \chi) = 1 - n/n_e = 1 - \frac{[-\log_e(\chi/\chi_m)]^{1/2}}{[-\log_e(\chi_e/\chi_m)]^{1/2}}, \qquad \text{(B 3}a, b\text{)}$$

which only includes information about the local layer maximum value. Differentiating (B 3b) with respect to χ gives the probability density of scalar dissipation values, conditioned on the layer maximum value as

$$\beta(\chi;\chi_m) = \frac{1}{2\chi[\log_e(\chi_m/\chi_e)\log_e(\chi_m/\chi)]^{1/2}}. \qquad \text{(B 4)}$$

Equation (B 4), shown in figure 32, gives the distribution of scalar dissipation rates for a given layer maximum value. If the distribution of layer maxima is known, then the distribution of scalar dissipation rates can be determined by noting that only layers having a maximum greater than or equal to χ will contribute, and then weighting with the probability that the layer maximum value will occur. Thus the probability density of scalar dissipation rates is

$$\beta(\chi) = \int_{\chi}^{\infty} \beta(\chi;\chi_m)\beta(\chi_m)\,\mathrm{d}\chi_m. \qquad \text{(B 5)}$$

We gratefully acknowledge discussions with Grétar Tryggvason in the Department of Mechanical Engineering and Applied Mechanics at The University of Michigan and with Robert Krasny in the Applied Mathematics group, also at Michigan. Additional discussions with Bill Willmarth, Luis Bernal, and Rayhaneh Akhavan at Michigan, as well as George Kosály at the University of Washington, are also gratefully acknowledged. Various parts of this work were supported by the Air Force Office of Scientific Research (AFOSR) under Grant No. 89-0541, by the Gas Research Institute (GRI) under Contract Nos. 5087-260-1443 and 5088-260-1692, and with discretionary funds provided by The University of Michigan.

REFERENCES

ANDREWS, L. C. & SHIVAMOGGI, B. K. 1989 The gamma distribution as a model for temperature dissipation in intermittent turbulence. *Phys. Fluids* A **2**, 105–110.

ANSELMET, F., GAGNE, Y., HOPFINGER, E. J. & ANTONIA, R. A. 1984 High-order velocity structure functions in turbulent shear flows. *J. Fluid Mech.* **140**, 63–89.

ASHURST, W. T., KERSTEIN, A. R., KERR, R. M. & GIBSON, C. H. 1987 Alignment of vorticity and scalar gradient in simulated Navier–Stokes turbulence. *Phys. Fluids* **30**, 2343–2353.

BATCHELOR, G. K. 1959 Small-scale variation of convected quantities like temperature in a turbulent fluid. Part 1. General discussion and the case of small conductivity. *J. Fluid Mech.* **5**, 113–133.

BATCHELOR, G. K. 1967 *An Introduction to Fluid Dynamics.* Cambridge University Press.

BATCHELOR, G. K., HOWELLS, I. D. & TOWNSEND, A. A. 1959 Small-scale variation of convected quantities like temperature in turbulent fluid. Part 2. The case of large conductivity. *J. Fluid Mech.* **5**, 134–139.

BATCHELOR, G. K. & TOWNSEND, A. A. 1949 The nature of turbulent motion at large wavenumbers. *Proc. R. Soc. Lond.* A **199**, 238–255.

BETCHOV, R. 1956 An inequality concerning the production of vorticity in isotropic turbulence. *J. Fluid Mech.* **1**, 497–504.

BETCHOV, R. 1974 Non-Gaussian and irreversible events in isotropic turbulence. *Phys. Fluids* **17**, 1509–1512.

BEVINGTON, P. R. 1969 *Data Reduction and Error Analysis for the Physical Sciences.* McGraw-Hill.

BIRINGEN, S. 1975 An experimental investigation of an axisymmetric jet issuing into a coflowing stream. *VKI Tech. Note* 110.

BORGAS, M. S. 1992 A comparison of intermittency models in turbulence. *Phys. Fluids* A **4**, 2055–2061.

BUCH, K. A. & DAHM, W. J. A. 1996 Experimental study of the fine scale structure of conserved scalar mixing in turbulent shear flows. Part 2. $Sc \approx 1$. *J. Fluid Mech.* (to be submitted).

BURGERS, J. M. 1948 A mathematical model illustrating the theory of turbulence. *Adv. Appl. Mech.* **1**, 171–199.

BURGERS, J. M. 1950 The formation of vortex sheets in a simplified type of turbulent motion. *Proc. Acad. Sci. Amst.* **53**, 122–133.

CARRIER, G. F., FENDELL, F. E. & MARBLE, F. E. 1975 The effect of strain rate on diffusion flames. *SIAM J Appl. Maths* **28**, 463–500.

CORRSIN, S. 1951 On the spectrum of isotropic temperature fluctuations in an isotropic turbulence. *J. Appl. Phys.* **22**, 469.

CORRSIN, S. 1962 Turbulent dissipation fluctuations. *Phys. Fluids* **5**, 1301–1302.

DAHM, W. J. A. & BUCH, K. A. 1989 Lognormality of the scalar dissipation pdf in turbulent flows. *Phys. Fluids* A **1**, 1290–1293.

DAHM, W. J. A. & DIBBLE, R. W. 1988 Coflowing turbulent jet diffusion flame blowout. *Proc. 22nd Intl Symp. on Combustion*, pp. 801–808. The Combustion Institute, Pittsburgh.

DAHM, W. J. A., SOUTHERLAND, K. B. & BUCH, K. A. 1991 Direct, high-resolution, four-dimensional measurements of the fine scale structure of $Sc \gg 1$ molecular mixing in turbulent flows. *Phys. Fluids* A **3**, 1115–1127.

DOWLING, D. R. & DIMOTAKIS, P. E. 1991 Similarity in the concentration field of gas-phase turbulent jets. *J. Fluid Mech.* **218**, 109–141.

ESWARAN, V. & POPE, S. B. 1988 Direct numerical simulations of the turbulent mixing of a passive scalar. *Phys. Fluids* **31**, 506–520.

FRISCH, U. & PARISI, G. 1985 In *Turbulence and Predictability in Geophysical Fluid Mechanics and Climate Dynamics* (ed. M. Ghil, R. Benzi & G. Parisi). North-Holland.

FRISCH, U., SULEM, P. & NELKIN, M. 1978 A simple dynamical model of intermittent fully developed turbulence. *J. Fluid Mech.* **87**, 719–736.

GIBSON, C. H. 1968*a* Fine structure of scalar fields mixed by turbulence. I. Zero-gradient points and minimal-gradient surfaces. *Phys. Fluids* **11**, 2305–2315.

GIBSON, C. H. 1968*b* Fine structure of scalar fields mixed by turbulence. II. Spectral theory. *Phys. Fluids* **11**, 2316–2327.

GIBSON, C. H., ASHURST, W. T. & KERSTEIN, A. R. 1988 Mixing of strongly diffusive passive scalars like temperature by turbulence. *J. Fluid Mech.* **194**, 261–293.

GIBSON, C. H. & LIBBY, P. A. 1972 On turbulent flows with fast chemical reactions. Part II – The distribution of reactants and products near a reacting surfaces. *Combust. Sci. Tech.* **8**, 29–35.

GIBSON, C. H., STEGEN, G. R. & WILLIAMS, R. B. 1970 Statistics of the fine structure of turbulent velocity and temperature fields measured at high Reynolds numbers. *J. Fluid Mech.* **41**, 153–167.

GURVICH, A. S. & YAGLOM, A. M. 1967 Breakdown of eddies and probability distributions for small-scale turbulence. *Phys. Fluids Suppl.* **10**, S59–S65.

HILL, R. J. 1978 Models of the scalar spectrum for turbulent advection. *J. Fluid Mech.* **88**, 541–562.

HILL, R. J. 1980 Solution of Howells' model of the scalar spectrum and comparison with experiment. *J. Fluid Mech.* **96**, 705–722.

KERR, R. M. 1985 Higher-order derivative correlations and the alignment of small scale structures in isotropic numerical turbulence. *J. Fluid Mech.* **153**, 31–58.

KOLMOGOROV, A. N. 1941 Local structure of turbulence in an incompressible fluid at very high Reynolds numbers. *C.R. Acad. Sci. URSS* **30**, 301–305.

KOLMOGOROV, A. N. 1962 A refinement of previous hypotheses concerning the local structure of turbulence in viscous incompressible fluid at high Reynolds number. *J. Fluid Mech.* **13**, 82–85.

KUO, A. Y. & CORRSIN, S. 1972 Experiments on the geometry of the fine-structure regions in fully turbulent fluid. *J. Fluid Mech.* **56**, 447–479.

LIEW, S. K., BRAY, K. N. C. & MOSS, J. B. 1981 A flamelet model of turbulent nonpremixed combustion. *Combust. Sci. Tech.* **27**, 69–73.

MACZYNSKI, J. F. J. 1962 A round jet in an ambient co-axial stream. *J. Fluid Mech.* **13**, 597–608.

MANDELBROT, B. B. 1974 Intermittent turbulence in self-similar cascades: divergence of high moments and dimension of the carrier. *J. Fluid Mech.* **62**, 331–358.

MANDELBROT, B. B. 1976 Intermittent turbulence and fractal dimension: kurtosis and the spectral exponent $5/3+\beta$. In *Turbulence and Navier–Stokes Equations* (ed. R. Teman). Lecture Notes in Mathematics, vol. **565**, pp. 121–145. Springer.

MENEVEAU, C. & SREENIVASAN, K. R. 1991 The multifractal nature of turbulent energy dissipation. *J. Fluid Mech.* **224**, 429–484.

NOVIKOV, E. A. & STEWART, R. W. 1964 Turbulent intermittency and the spectrum of fluctuations of energy dissipation. *Izv. Akad. Nauk. SSSR, Geofiz.* no. 3, 408–413.

OBUKHOV, A. M. 1949 Structure of the temperature field in a turbulent flow. *Izv. Acad. Nauk SSSR, Geogr. i Geofiz* **13**, 58–69.

OBUKHOV, A. M. 1962 Some specific features of atmospheric turbulence. *J. Fluid Mech.* **13**, 77–81.

OTTINO, J. M. 1982 Description of mixing with diffusion and reaction in terms of the concept of material surfaces. *J. Fluid Mech.* **114**, 83–103.

OTTINO, J. M. 1989 *The Kinematics of Mixing: Stretching, Chaos, and Transport.* Cambridge University Press.

PETERS, N. 1984 Laminar diffusion flamelet models in non-premixed turbulent combustion. *Prog. Energy Combust. Sci.* **10**, 319–339.

PETERS, N. & WILLIAMS, F. A. 1983 Liftoff characteristics of turbulent jet diffusion flames. *AIAA J.* **21**, 423–429.

POPE, S. B. & CHENG, W. K. 1988 The stochastic flamelet model of turbulent combustion. *Proc. 22nd Intl Symp. Combustion.* The Combustion Institute, Pittsburg.

PRASAD, R. H. & SREENIVASAN, K. R. 1990 Quantitative three-dimensional imaging and the structure of passive scalar fields in fully turbulent flows. *J. Fluid Mech.* **216**, 1–34.

REICHARDT, H. 1964 Turbulente Strahlausbreitung in gleichgerichteter Grundströmung. *Forsch. Ing. Wes.* **30**, 133–139.

RICHARDSON, L. F. 1920 The supply of energy from and to atmospheric eddies. *Proc. R. Soc. Lond.* A **97**, 354–373.

ROGERS, M. M. & MOIN, P. 1987 The structure of the velocity field in homogeneous turbulent flows. *J. Fluid Mech.* **176**, 33–66.

SHE, Z.-S., JACKSON, E. & ORSZAG, S. A. 1990 Intermittent vortex structures in homogeneous isotropic turbulence. *Nature* **344**, 226–228.

SHERMAN, F. S. 1990 *Viscous Flow.* McGraw-Hill.

SIGGIA, E. D. 1981 Numerical study of small scale intermittency in three-dimensional turbulence. *J. Fluid Mech.* **107**, 375–406.

SREENIVASAN, K. R. 1991 Fractals and multifractals in fluid turbulence. *Ann. Rev. Fluid Mech.* **23**, 539–600.

TAYLOR, G. I. 1935 Statistical theory of turbulence. *Proc. R. Soc. Lond.* A **151**, 421–478.

TENNEKES, H. 1968 Simple model for the small-scale structure of turbulence. *Phys. Fluids* **11**, 669–671.

TOWNSEND, A. A. 1951 On the fine-scale structure of turbulence. *Proc. R. Soc. Lond.* A **208**, 534–542.

VAN ATTA, C. W. & CHEN, W. Y. 1970 Structure functions of turbulence in the atmospheric boundary layer over the ocean. *J. Fluid Mech.* **44**, 145–159.

VAN ATTA, C. W. & YEH, T. T. 1975 Evidence for scale similarity of internal intermittency in turbulent flows at large Reynolds numbers. *J. Fluid Mech.* **71**, 417–440.

WARE, B. R., CYR, D., GORTI, S. & LANNI, F. 1983 In *Measurements of Suspended Particles by Quasi-Elastic Light Scattering* (ed. B. E. Dahneke), p. 255. Wiley.

YAMAMOTO, K. & HOSOKAWA, I. 1988 A decaying turbulence pursued by the spectral method. *J. Phys. Soc. Japan* **57**, 1532–1535.

YEUNG, P. K., GIRIMAJI, S. S. & POPE, S. B. 1989 Straining and scalar dissipation on material surfaces in turbulence: implications for flamelets. *Combust. Flame* **79**, 340–365.